ACS Electrochemistry

pubs.acs.org/electrochem

Article

Carbonaceous Interlayers as Contact Mediators for Sodium Electrodeposition in "Anode-Free" Solid-State Batteries

Maya Ziegler, Till Ortmann, Chantal Glatthaar, Jona-Matteo Werner, Vipin K. Singh, Boris Mogwitz, Janis K. Eckhardt, Bernd M. Smarsly, Linda F. Nazar, Marcus Rohnke, and Jürgen Janek*

Cite This: *ACS Electrochem.* 2026, 2, 1887−1903

Read Online

ACCESS | Metrics & More | Article Recommendations | Supporting Information

ABSTRACT: Interfacial contact limitations challenge reversible, high-rate sodium deposition in "anode-free" sodium solid-state batteries and motivate interlayer-based interface engineering strategies. Here, we systematically investigate how microstructural properties of non-graphitic carbon interlayers, i.e., the structural arrangement of graphene domains, particle size, and network porosity, govern the early stages of sodium nucleation and growth in NaSICON-based half-cells ($\leq$ 750 μAh·cm^{-2}). Comparing coarse- and fine-particle hard carbon and carbon black interlayers (23–1200 nm), prepared by tape-casting, shows that finer, more compactable carbons improve solid electrolyte contact and promote uniform lateral sodium growth while suppressing dendrites. Focused ion-beam scanning electron microscopy and energy-dispersive X-ray spectroscopy confirm that sodium electrodeposition occurs predominantly at the interlayer|SE interface, with partial sodium insertion into the carbon framework. Mechanical interlocking between the compliant carbon interlayer and a rough solid electrolyte surface enhances adhesion, stabilizes interfacial contact, prevents delamination of the carbon-coated current collector, and promotes laterally extended sodium growth. These findings elucidate how tailored interlayer microstructure and interfacial mechanics govern sodium electrodeposition behavior. Carbonaceous interlayers mediate interfacial contact and homogenize current distribution at the current collector|solid electrolyte interface, thereby defining design principles for solid-state sodium batteries during electrodeposition.

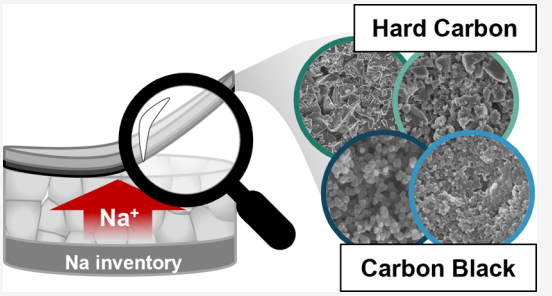

KEYWORDS: *sodium metal, reservoir-free cell, carbon interlayer, adhesion, mechanical interlocking*

INTRODUCTION

Sodium-ion batteries (SIBs) serve as important alternatives and complements for lithium-ion batteries (LIBs) to overcome shortages and price volatility as the global energy and energy storage demand rises.[1] At the negative electrode, carbon materials, particularly hard carbons (HCs), have become the preferred choice for liquid electrolyte-based SIBs due to their good sodium storage capability and stability upon sodiation/desodiation.[2−5] Unlike graphite, these non-graphitic carbon materials feature two-dimensionally ordered graphene-sheet domains and exhibit both an inherent and deliberately introducible porosity (via templating),[6] which enables sodium accommodation through adsorption, insertion, and filling of open- and closed-type micro-/mesopores.[7,8] Like graphite, they also frequently suffer from alkali metal plating. Their reversible capacity (C_g ~ 200–350 mAh·g^{-1}) and the resulting specific energy of full SIB cells (E_g ~ 100–175 Wh·kg^{-1}) are inherently limited.[2,9]

To overcome this limitation and attain higher energy densities, there is interest in employing sodium metal electrodes (C_g = 1,165 mAh·g^{-1}) instead of host material frameworks. Most liquid electrolyte-based systems exhibit inherent instability towards the sodium metal electrode, resulting in solid electrolyte interphase (SEI) formation, as well as dendritic growth upon electrodeposition.[10] Thus, solid electrolytes (SEs), such as NaSICON materials and Na-β″-alumina,[11] have garnered significant attention due to their chemical and mechanical stability against the sodium metal electrode and enhanced safety by replacing flammable liquid electrolytes (E_g ~ 230 Wh·kg^{-1}).[12,13] By utilizing the accessible sodium content stored in the sodiated cathode active material – forming the sodium metal electrode *in situ* during charging at the current collector|solid electrolyte interface (CC|SE) – this approach can further optimize the energy density of the battery (E_g ~ 250 Wh·kg^{-1}). Simultaneously, it avoids the use of sodium metal foils and simplifies manufacturing.[14,15] This cell configuration is commonly referred to as "anode-free", or more

Received: March 26, 2026
Revised: May 18, 2026
Accepted: May 27, 2026
Published: June 15, 2026

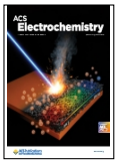

accurately described as a zero-excess or reservoir-free cell (RFC).[14,16,17]

In RFCs, the electrodeposition of sodium at the CC|SE interface ideally proceeds in a layer-by-layer mode, thus generating dense uniform sodium films covering the entire electrode in both area and thickness. However, in practice, RFCs often face morphological instabilities due to non-uniform deposition, which manifests in whisker or island formation.[16,18−21] This leads to interfacial gaps due to delamination of the CC, as well as dendrite growth. The former results in a reduced electrochemically active area and increases the cell resistance because geometric current constriction causes an additional interface-related contribution,[22,23] while the latter poses a risk of short-circuiting the cell.

To address these issues, functional interlayers are often introduced between the SE and CC. The most established interlayers for RFCs include metal alloying, carbonaceous, and nanocomposite interlayers.[24−29] While the use of interlayers is a well-established strategy for lithium-based systems,[24−29] research on their application in solid-state sodium systems is still in its infancy and has thus far mainly focused on metal alloying interlayers.[30,31] These ideally very thin interlayers tend to ensure conformal contact and thereby homogenize ion flux, while ideally preserving their mesostructural integrity over multiple cycles.[32] Metal alloying interlayers can effectively guide electrodeposition, but are costly. They also often suffer from structural degradation, since the alloying element is gradually depleted at the SE interface and undergoes significant volume changes upon alloying.[25,26] Interlayers with a carbon-based matrix, by contrast, are low-cost, scalable, and structurally robust.[33]

Carbon-containing interlayers introduce two possible sodium deposition sites, namely the CC|interlayer and interlayer|SE interface. Since sodium deposition at the CC|interlayer interface prevents direct Na|SE contact and thus SE degradation, this interface is the preferred growth site. Generally, the conductive properties of the interlayer and the strength of interfacial adhesion govern the preferential deposition position.[24,29] If adhesion of the interlayer to the CC is weaker than to the SE, while sodium(-ion) transport across the interlayer remains sufficiently fast, electrodeposition preferentially occurs at the CC|interlayer interface. In lithium-based systems, numerous parameters have already been shown to influence the plating location, including the nature of the carbon, i.e., allotrope,[27,32] porosity,[29] and electrical conductivity,[34] as well as processing parameter and operating protocols during electrodeposition, including the thickness of the interlayer,[35] temperature,[24,27] current density,[36] and fabrication pressure.[37]

A pioneering example of a carbon-based interlayer for sodium solid-state cells was presented by Sun et al. who designed a composite layer containing ferroelectric $BaTiO_3$ particles dispersed within a Super P carbon black (CB) matrix.[38] A dense sodium layer was formed, which was speculated to result from an improved sodium ion distribution at the interface driven by the local piezoelectric field of the $BaTiO_3$ particles. The sole carbon-based interlayer without $BaTiO_3$ was only briefly investigated, leaving the specific role of the carbon matrix open to further exploration. It is unclear whether carbon merely acts as a mechanically and electronically conductive buffer, or whether its microstructural properties play an active role in governing nucleation behavior and subsequent growth of sodium metal. This raises the central question of whether carbon materials can actively facilitate sodium nucleation, beyond their conventional role as anode host materials in SIBs, and promote its homogeneous electrodeposition in solid-state cells.[39]

To answer this question, here we systematically investigate how the microstructure and particle-level deformability of carbonaceous interlayers govern sodium nucleation and growth in reservoir-free solid-state half-cells employing a NaSICON-type SE. To this end, both HC and CB materials with coarse- and fine-particle size are compared to elucidate the role of microstructural parameters, i.e., structural order of the graphene domains on the nanoscale, and particle size and network porosity on the mesoscale. The study combines electrochemical analysis during electrodeposition, including electrochemical impedance spectroscopy (EIS), with focused ion-beam secondary electron microscopy (FIB-SEM), and energy-dispersive X-ray spectroscopy (EDS) characterization to correlate interfacial morphology and composition with cell performance. The discussion proceeds from (i) the structural characterization of the carbon materials, through (ii) the analysis of sodium electrodeposition and deposit morphology with carbonaceous interlayers, to (iii) the optimization of the interlayer|SE interface via a mechanical interlocking strategy. Together, our results reveal how carbon microstructure, SE surface topography, and interfacial mechanics jointly dictate sodium nucleation and growth. Importantly, this establishes the underlying structure–property–performance relationships that guide interlayer design of low-cost, scalable, and structurally robust interlayers for sodium-based RFCs.

■ RESULTS AND DISCUSSION

Carbonaceous Interlayers

Carbon Types for Interlayer Fabrication. Sodium storage in carbon frameworks can proceed through two competing processes: accommodation into the carbon material and metallic plating on its surface.[7] Sodium can be housed through adsorption on defects and edges, insertion between graphene layers, and filling of pores.[40] The process can be tuned by tailoring both the nanoscale microstructural carbon properties, e.g., graphene interlayer spacing as well as graphene layer extent, and the mesoscale microstructural characteristics of the carbon interlayer network that include particle size,[41] morphology, and their packing arrangement.[42,43] As part of this study, we investigated non-graphitic carbons as their sodium storage capability may facilitate nucleation and promote uniform deposition. Both, HC and CB materials with coarse (c) and fine (f) particle size considered here, denoted as HC_c/CB_c and HC_f/CB_f, belong to this class. They are characterized by a turbostratic structure composed of two-dimensional ordered graphene-like layers which are varying in their lateral extension as well as orientation, contain structural defects like sp^3-hybridized carbon atoms, and are arranged in stacks (Figure S1).[8,44] Within this class of carbons, their distinctions arise primarily from morphology and precursor origin.[5,45]

Nanoscale Microstructural Properties of the Carbon Materials. The common turbostratic structure of the carbon materials is confirmed by characteristic scattering patterns exhibiting (00*l*) and (*hk*) reflections instead of general (*hkl*) reflections. Fitting of the experimental scattering data (Figure S2) allowed the calculation of quantitative microstructure parameters that describe the extension of graphene layers and their stacking (Table 1).[46] This analysis reveals that within each type of carbon the fundamental nanoscale microstructural

https://doi.org/10.1021/acselectrochem.6c00121
ACS Electrochem. 2026, 2, 1887−1903

Table 1. Nanoscale Microstructural Parameters of the Coarse and Fine HC_c, HC_f, CB_c, and CB_f Interlayer Materials Derived from Quantitative Fitting of Wide-Angle X-ray Scattering Data Using the Ruland and Smarsly Algorithm[46]

	HC_c	HC_f	CB_c	CB_f
average interlayer spacing a_3/Å	3.59	3.59	3.53	3.54
standard deviation of first-neighbor distribution σ_1	0.14	0.11	0.08	0.17
standard deviation of interlayer spacing σ_3/Å	0.58	0.24	0.30	0.59
average C−C bond length l_{cc}/Å	1.409	1.411	1.416	1.415
average graphene layer extent L_a/Å	23.9	23.8	31.4	25.0
average stack height L_c/Å	8.2	6.4	19.7	18.2

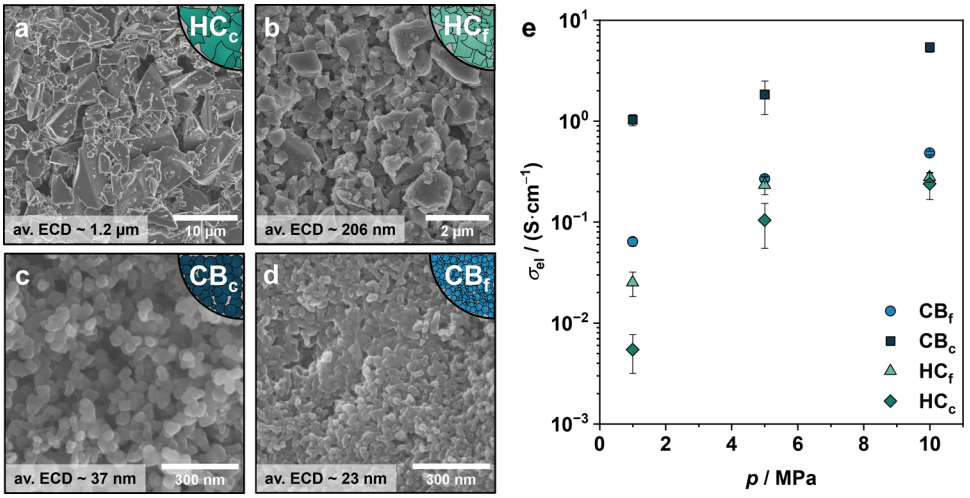

Figure 1. (a–d) Top-view SEM images of tape-casted coarse and fine HC_c/HC_f-based (a, b) and CB_c/CB_f-based (c, d) interlayers, highlighting the differences in average primary particle size and resulting mesoscale microstructure (note the different scale bars). The CB_f-based interlayer exhibits pronounced particle agglomeration, which is attributed to particle coverage by the added binder. (e) Electronic conductivity of the different carbon materials measured in a steel|Cu|carbon|Cu|steel configuration using a four-point probe geometry as a function of pressure.

parameters, i.e., interlayer spacing, C–C bond length, and average stack height, are very similar. Compared to the HC materials, the CB materials exhibit slightly smaller interlayer spacings (a_3) as well as significantly larger graphene layer extents (L_a) and stack heights (L_c), indicative of a more regular stacking of graphene layers (Figure S1). These parameters already suggest the extent of different storage mechanisms. The less ordered HC materials, with their larger interlayer spacings and heterogeneous stacking, are expected to offer higher sodium insertion and adsorption capacity compared the more ordered CB materials. Porosity analysis of the investigated carbon materials was not performed as pore filling is generally associated with the low-potential plateau region in SIBs.[47] However, in solid-state systems a potential drop is observed after the sloping region,[37,38] which indicates that immediate metal nucleation occurs and suggests that pore filling is a secondary process in solid-state cells.

Mesoscale Microstructural Properties of the Carbon Materials. To further elucidate the carbons' mesoscale microstructural architecture in the form of interlayers, SEM analysis of the tape-casted interlayers was performed (Figure 1a–d). It reveals that both HC samples consist of irregular, shard-like particles on the micron scale (Figure S3; average equivalent circular diameter (ECD) for coarse HC_c av. ECD(HC_c) ∼ 1.2 µm and for fine HC_f av. ECD(HC_f) ∼ 206 nm). In contrast, both CB samples are composed of nanosized, quasi-spherical primary particles (av. ECD(CB_c) ∼ 37 nm; av. ECD(CB_f) ∼ 23 nm) that agglomerate into dense, interconnected networks upon addition of binder and subsequent tape-casting onto aluminum. Notably, the finer CB_f represents a post-oxidized CB material with an increased surface oxygen content, which may influence its interaction with the binder, SE, and electrodeposited sodium.[48]

To assess how the mesoscale architecture of the carbonaceous interlayers governs their transport properties, specifically electronic transport, pressure-controlled four-point conductivity measurements were carried out (Figure 1e).[49] Because electrochemical reduction of sodium ions can only proceed at locations where ionic and electronic transport pathways intersect, the distribution of electronic conduction paths can influence the plating position.[29,34] Owing to their nanoscale dimensions and homogeneous packing, CB networks establish continuous conductive pathways even at low applied pressures (∼ 1 MPa), while the coarser and more angular HC particles require substantially higher pressures (≥ 5 MPa) to achieve comparable interparticle contact and network connectivity. The measured conductivity reflects the electronic conductivity and is often simply referred to as electric conductivity,[49,50] as the diffusion of sodium ions and thus the ionic contribution is negligible in carbon materials ($\tilde{D}_{Na}$ ∼ 10^{-9}–10^{-12} $cm^2 \cdot s^{-1}$).[9] The generally higher electronic conductivity observed for CB_c relative to CB_f can be attributed to its more ordered assembly of graphene layers as indicated by the larger graphene layer extent (L_a: 31.4 Å vs 25.0 Å). Importantly, previous findings

https://doi.org/10.1021/acselectrochem.6c00121
ACS Electrochem. 2026, 2, 1887−1903

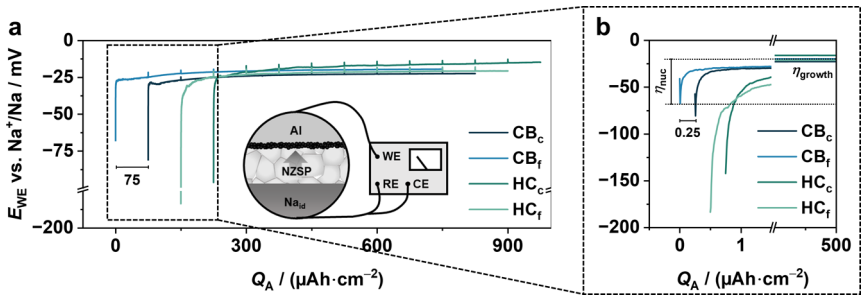

Figure 2. (a) Potential profiles of half-cells recorded during cathodic sodium deposition at a current density of 0.3 mA·cm^{-2} under an applied stack pressure of 1.5 MPa up to an areal capacity Q_A of 750 μAh·cm^{-2}. The profiles are horizontally offset by 75 μAh·cm^{-2}. The schematic illustrates the half-cell configuration used in this study (Al|interlayer|NZSP|Na_{id}). Electrodeposition was periodically interrupted every 75 μAh·cm^{-2} for EIS measurements, giving rise to the small spikes observed in the potential profiles. (b) Enlarged view of the nucleation regime highlighting the different nucleation overpotentials (horizontal offset: 0.25 μAh·cm^{-2}).

by Pantea et al. demonstrate that electronic conductivity is governed primarily by the structural arrangement and extension of graphene layers rather than by surface chemical modification, a conclusion that is supported by the trend observed here.[49,50]

The comparable nanoscale microstructural characteristics of the CB and HC materials enable meaningful comparison for each carbon type in the following, with the main distinctions arising from their mesoscale properties, including particle size and morphology. These parameters can critically influence the effective interfacial contact and current distribution during sodium electrodeposition in solid-state cells.

Potential Profiles. A half-cell with a sodium counter electrode (CE) was employed to investigate the difference in sodium deposition with HC- and CB-based interlayers from a NaSICON-type SE, $Na_{3.4}Zr_2Si_{2.4}P_{0.6}O_{12}$ (NZSP, Figure S4). Here, the CE simultaneously serves as reference electrode (RE; Figure 2a).[51,52] The corresponding potential profiles during electrodeposition at 0.3 mA·cm^{-2} and a low stack pressure of 1.5 MPa are shown in Figure 2a for an areal capacity (Q_A) up to 750 μAh·cm^{-2}. The potential profiles for all carbonaceous interlayers exhibit a characteristic potential drop followed by a potential plateau regime, corresponding to sodium nucleation and metal growth similar to recent findings.[38] In contrast to half-cells without an interlayer, where the aluminum CC was isostatically cold-pressed to the SE (Figure S5),[20] the introduction of carbonaceous CB- or HC-based interlayers ensured stable electrodeposition in early stages of sodium deposition ($\leq$ 750 μAh·cm^{-2}) without short-circuiting. Bare CC systems, either through diffusion-bonding of an aluminum CC or thermal evaporation of a copper CC required a high-temperature treatment for stable electrodeposition.[16,20] By contrast, our results here were achieved without any manufacturing step involving a thermal, energy-intensive step for CC attachment. Moreover, carbon coatings of CC foils are already an established industrial process, rendering this approach scalable and cost-effective compared to high-temperature treatments or costly metallic alloying interlayers.[30,31]

The difference between the initial potential drop and the plateau regime is defined as the nucleation overpotential η_{nuc} as shown in Figure 2b.[53] For HC-based interlayers, both coarse and fine, the nucleation overpotential of the HC materials, cannot be resolved with the chosen sampling rate (10 Hz) of the potential measurement, suggesting that nucleation is fast. In contrast, CB-based interlayers show nucleation overpotentials with $\eta_{nuc} = (68 \pm 9)$ mV and (51 ± 2) mV for CB_c and CB_f, respectively (Figure S6). The actual nucleation overpotential might be obscured due to averaging of data points. However, the generally higher nucleation overpotential for CB_c-based compared to CB_f-based interlayers is attributed to a smaller effective contact area and higher local exchange current densities associated with the larger carbon particle size and thus a lower number of microcontacts.[54]

Initial accommodation of sodium into the carbon prior to metal nucleation, which is the "classical" view on sodium metal storage in carbon, was not evident for the investigated carbonaceous interlayers, as no sloping regime preceding the potential drop is observed in the potential profiles. This behavior is attributed to the limited effective interfacial contact area between the carbon interlayer and the SE, which concentrates the applied current at discrete microcontacts.[53,55] At locally concentrated current densities immediate sodium plating is favored,[35,56,57] whereas at sufficiently low and homogeneously distributed current densities, sodium adsorption and insertion into carbon can precede metal nucleation. Comparable behavior has been reported for carbon frameworks used as anode active materials in liquid electrolyte-based batteries.[7,43] There, high charging rates suppress ion accommodation in the carbons and instead promote metal plating on the carbon surface or within its porous network.[58,59] This owes to limited ion diffusion within the carbon ($\widetilde{D}_{Na} \sim 10^{-9}$–$10^{-12}$ cm^2·s^{-1}) and locally concentrated current densities analogous to the conditions here.[9]

Furthermore, the potential profiles reveal distinct growth overpotentials η_{growth}, differing not only between interlayer types but also among half-cells employing the same interlayer (up to 6 mV for HC_f, Figure S6). These differences likely stem from variations in interfacial contact area and spatial distribution, and thus from differences in the active conductive volume within the SE.[16] Because the absolute cell voltage is also influenced by the CE area, the observed values should be interpreted as qualitative indicators rather than being directly comparable. Nevertheless, the differences in η_{growth} suggest slightly different sodium deposition behavior across the cells, motivating a FIB-SEM cross-sectional analysis of the resulting electrodeposited sodium morphology and interfacial structure, which is described below.

Cross-Sectional Analyses of Electrodeposited Sodium. Figure 3 shows the FIB cross-sections of half-cells with carbonaceous interlayers both in the pristine state and following electrodeposition. Because such cross-sections represent only a restricted local field of view, multiple cross-sections were

https://doi.org/10.1021/acselectrochem.6c00121
ACS Electrochem. 2026, 2, 1887−1903

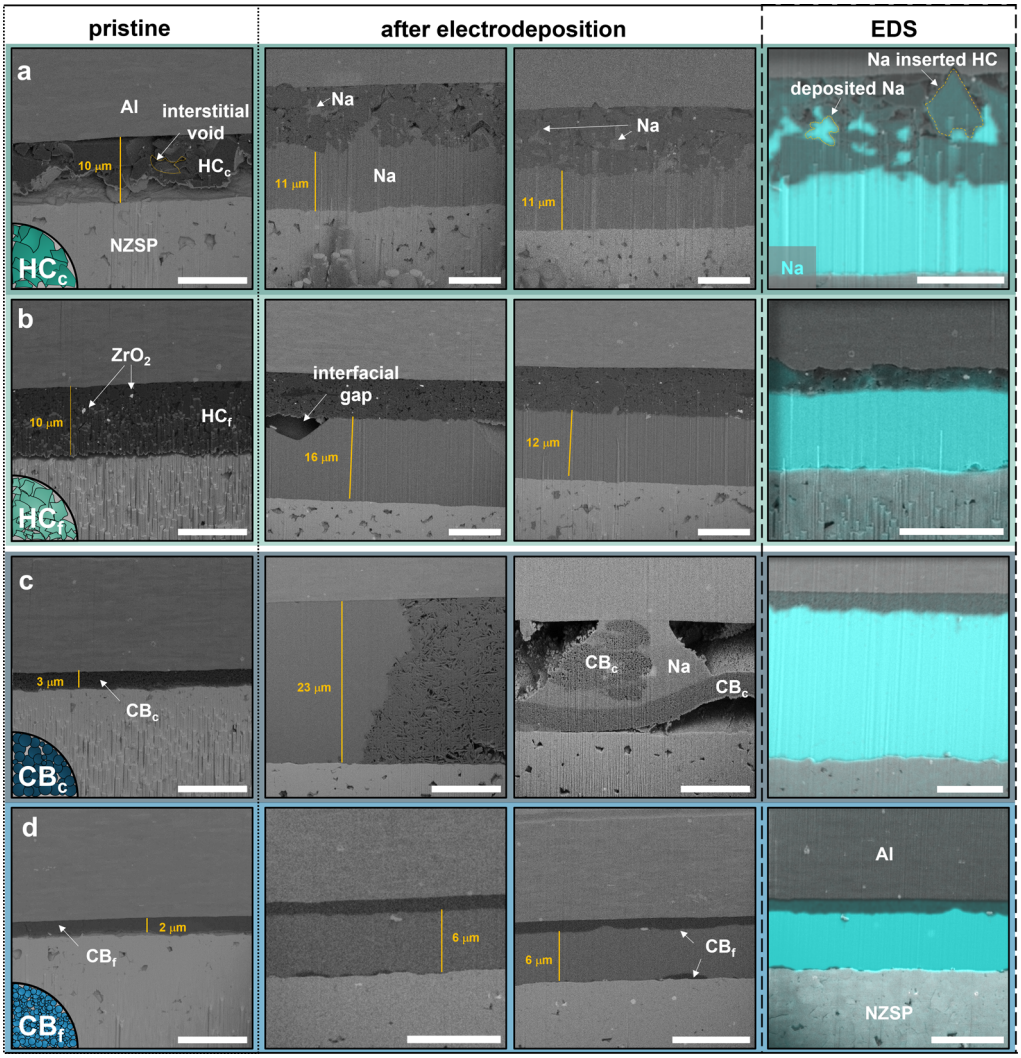

Figure 3. FIB-SEM cross-sections of half-cells with Al|interlayer|NZSP|Na_{id} configuration in the pristine state and after cathodic deposition of 750 μAh·cm^{-2} sodium metal at 0.3 mA·cm^{-2} with an applied stack pressure of 1.5 MPa for (a) HC_c-based interlayers, (b) HC_f-based interlayers, (c) CB_c-based interlayers, and (d) CB_f-based interlayers. Sodium accommodation following nucleation into HC is more pronounced than for CB interlayer materials. Scale bars equal 10 μm.

cut, often revealing gaps between the SE and the carbon-coated CC (Figure S7). However, specific areas where sodium was electrodeposited were intentionally analyzed to gain deeper insights into its morphology and sodium accommodation in the carbonaceous interlayer.

HC-Based Interlayers. The HC_c-based interlayer consists of irregular, micrometer-sized particles that form a loosely packed and highly porous network with large interstitial voids (Figure 3a). Due to the coarse particle morphology, only few discrete contact points are established with the SE. In contrast, the HC_f interlayer exhibited a denser and more homogeneous packing (Figure 3b), owing to its smaller particle size which enhances compactability and reduces the interstitial void volume. Nevertheless, the image shows that the contact with the SE remains limited, likely due to poor adhesion, with a small gap present at the interface. Minor zirconia contamination from the milling media is visible for HC_f-based interlayers, but expected to be electronically insulating and chemically inert under the applied conditions. The thickness of both HC interlayers extends to approximately 10 μm.

After electrodeposition, sodium appears as a dense deposit at the interlayer|SE interface. This behavior can be rationalized by considering both charge transport through the interlayer and adhesion of the interfaces as schematically depicted in Figure 4. While electron transport through the carbon interlayer is fast ($\sigma_{el} \sim 0.1$–10 S·cm^{-1}; Figure 1d), ionic transport through the interlayer is comparatively sluggish ($\tilde{D}_{Na} \sim 10^{-9}$–$10^{-12}$ cm^2·s^{-1}),[9] favoring sodium ion reduction at the SE interface. In addition, the site for nucleation and continuous electrodeposition thereafter is governed by relative interfacial adhesion strengths.[24,29] Peel-off tests showed that the interlayer adheres more weakly to the SE than to the CC, demonstrating that the work of adhesion W_{ad}, a macroscopic interfacial property dictated by the adhesion strengths and the number of microcontacts at the interface, is weaker between interlayer|SE than CC|interlayer interface ($W_{ad,II} < W_{ad,I}$). Thus, the carbon interlayers act as electronically and mechanically compliant extensions of the CC (σ_{el}(Al) $\sim 10^5$ S·cm^{-1}), directing electrons towards the SE interface where sodium ions are reduced. Compared with a dense metal foil CC, the carbon-based

https://doi.org/10.1021/acselectrochem.6c00121
ACS Electrochem. 2026, 2, 1887−1903

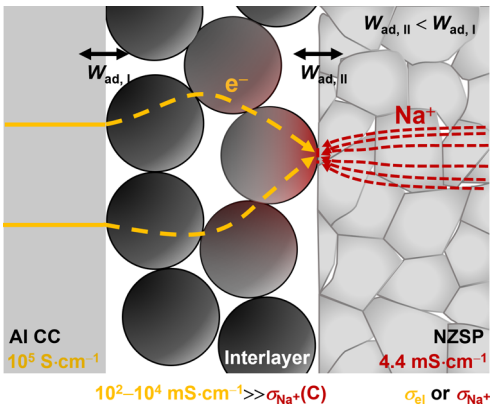

Figure 4. Scheme of interfacial adhesion and charge transport directing sodium electrodeposition at the interlayer|SE interface.

interlayers provide superior mechanical compliance, which facilitates improved interfacial conformity with the SE. We would like to note, that this concept is generally applicable for nonreactive or weakly-interacting interlayers. As in the case of reactive interlayer, e.g., alloy-forming or conversion-type, reaction upon sodiation could change the relative adhesion of the interfaces due to volume changes and thus the plating position and is expected to be more dynamic.

Assuming a film-like, layer-by-layer sodium deposition, the applied areal capacity (750 μAh·cm^{-2}) corresponds to a nominal sodium thickness of 6.6 μm. Deviations from this value can result from non-uniform sodium growth, such as the formation of isolated metal islands, whiskers, or dendritic filaments across the electrode. Indeed, in HC_c half-cells, sodium nucleated locally at limited contact sites and grew predominantly vertically beneath the interlayer, resulting in deposits considerably thicker (∼ 11 μm) than expected for ideal layer-by-layer growth (Figure 3a). This uneven vertical expansion induced stresses and caused partial delamination of adjacent regions of the carbon-coated CC (Figure S7a).[60] In addition, sodium infiltrated the large interstitial voids of the HC_c framework via surface diffusion and creep-assisted deformation, thereby converting the nominally two-dimensional interlayer|SE interface into an effectively three-dimensional sodium network with a markedly increased effective interfacial contact area.[61,62]

The HC_f interlayer, though more compact, also showed sodium deposition at the interlayer|SE interface. However, this was accompanied by the absence of sodium deposition in interstitial voids and by gap formation between the deposited sodium and the interlayer (Figure 3b). This observation raises the question of whether a partially sodiophobic surface of the HC_f-based interlayer may promote the development of such interfacial gaps. Furthermore, no clear evidence of dendrite penetration was observed in FIB-SEM cross-sections of the HC-based interlayers. However, light microscopy of polished SE surfaces for both HC-based interlayers after electrodeposition reveals small, dark-grey spots, which are tentatively attributed to localized dendritic filaments that were not captured within the analyzed cross-sections (Figure S8).

Elemental distribution of cross-sections analyzed by EDS show that sodium is present within the interlayers after electrodeposition, indicating partial accommodation of sodium in the carbon framework (Figure 3a,b). As the potential profiles show an immediate potential drop without a preceding sloping region, we infer that sodium accommodation into the carbon material occurs subsequently to nucleation, i.e., after sodium metal has formed at the interlayer|SE interface. The observed sodium signal within the carbon layers thus likely originates from post-nucleation diffusion into the carbon matrix from adjacent metal deposits.

Both HC_c and HC_f interlayers exhibited a locally increased sodium signal ($K_{\alpha 1,2}$) within the carbon particles, indicating sodium accommodation in the carbon material. This is consistent with the nanoscale microstructural parameters of the materials derived from X-ray scattering analysis that indicate the feasibility of sodium adsorption on defects or insertion between the graphene layers. In contrast, sodium infiltration into interstitial voids on the order of > 100 nm of the carbon network was observed only for the coarse particle HC_c interlayers, where distinct sodium deposits form within the interparticle porosity network thereby forming a three-dimensional sodium network. Sodium likely reaches these regions through a combination of surface diffusion on carbon particles (E_a ∼ 0.1 eV) and creep-mediated deformation of sodium metal, which together enable gradual infiltration into accessible interstitial void spaces.[9,42,63] Subsequent sodium insertion and distribution inside the carbon presumably occurs through diffusion between graphene layers (E_a ∼ 0.2–0.3 eV),[63] accounting for an observed sodium signal extending up to 5–6 μm into the interlayer.

CB-Based Interlayers. For CB, the cross-sectional analysis displayed in Figure 3c,d, reveal thinner and smoother interlayers (∼ 2–3 μm) than the HC-based counterparts (∼ 10 μm) due to better particle-to-particle densification. Furthermore, the CB interlayers exhibited a more intimate and conformal contact with the SE, as the fine carbon network adapts closely to the surface topography. Variations in interfacial conformity of the interfacial contact were observed between the various interlayers, indicating that the degree of physical adaptation to the SE surface strongly depends on the particle size of the carbon. Interlayers composed of very small carbon particles exhibit a higher degree of mechanical compliance. This is due to the increased number of interparticle contact points and the ability of the particle network to undergo localized rearrangement and plastic accommodation under applied pressure. Such behavior allows the interlayer to adapt to the surface topography of the SE, filling interfacial voids/asperities and improving contact homogeneity and interfacial integrity.

After electrodeposition, the CB_c interlayer exhibited pronounced mechanical degradation, manifested in rupturing and interlayer accumulation resulting from stress build-up during sodium electrodeposition owing to volume expansion (Figure 3c). The resulting local sodium deposits were considerably thicker (up to 23 μm) than expected for layer-by-layer growth, indicating non-homogeneous island and whisker-type deposition. In addition to dense deposits, regions with a fibrous morphology were also observed.[64]

By contrast, the CB_f interlayer largely retained its structural integrity, with only thin remnants of the carbonaceous interlayer remaining at the SE interface beneath the dense sodium deposit (Figure 3d). This demonstrates that a thin CB_f-based interlayer enables the formation of a dense sodium deposit suitable for RFC operation, marking a clear improvement over the others. The preserved integrity of the interlayer was further confirmed by post-deposition observations. When the CC was peeled off, the carbonaceous interlayer remained attached to

https://doi.org/10.1021/acselectrochem.6c00121
ACS Electrochem. 2026, 2, 1887−1903

the CC in regions where no sodium grew underneath (Figure S9). In contrast, in areas containing sodium deposits, the interlayer was found on top of the sodium layer, without any noticeable material loss. This confirms that deposition occurs almost exclusively at the interlayer|SE interface without significant detachment or degradation of the carbon layer. Although the sodium thickness in the analyzed cross-sections (~ 6 μm) is close to the theoretical value expected for layer-by-layer growth (6.6 μm), light microscopy revealed small island-like features, indicating local inhomogeneities in surface coverage (Figure S10).

EDS analysis shows that CB-based interlayers (~ 2–3 μm) display a more uniform but overall weaker sodium signal than HC (Figure 3c,d), reflecting their intrinsically lower capacity for sodium storage due to their nanoscale microstructural properties. However, due to the limited lateral resolution of EDS, we cannot unambiguously distinguish whether the detected sodium in CB originated from deposition in interstitial voids or accommodation in the carbon particles themselves. The slightly higher sodium content observed for fine CB_f compared with coarse CB_c, likely stems from its oxygen-rich surface, which promotes sodium adsorption through energetically favorable C−O−Na interactions.[48]

Impedance Evolution. Overall, FIB-SEM analyses demonstrate that the resulting sodium morphology depends on how intimate is the contact the interlayer establishes with the SE in the pristine state. To probe the dynamic evolution of this interfacial contact in more detail during electrodeposition, electrochemical impedance spectroscopy was performed, enabling a qualitative assessment of the evolution of interfacial resistance and sodium coverage. All impedance spectra in Figure 5 are displayed in Nyquist plot representation for the half-cell configuration CC|interlayer|NZSP|Na_{id}. These exhibit an offset along the Re(Z) axis, which originates from bulk ionic transport within the SE. The corresponding relaxation process occurs at frequencies around f_{apex} ~ 560 MHz at room temperature and therefore lies well outside the accessible frequency range of 7 MHz to 100 Hz, preventing its experimental resolution.[65] In addition, a contribution ascribed to grain boundary transport appears in the high frequency region (f_{apex} = 1.5 MHz). Together, these two features represent the SE.

In the pristine state, the impedance spectra exhibit a characteristic blocking behavior with pronounced charge build-up at the working electrode (WE) in the high-to-mid-frequency region (Figure 5). For HC-based cells, this blocking response was already evident in the high-frequency regime ($f(HC_c) \leq 3$ MHz; $f(HC_f) \leq 0.8$ MHz), whereas for CB-based cells it emerged predominantly at mid frequencies ($f \leq 0.2$ MHz). This shift indicates substantial differences in the contact geometry at the CC|interlayer|SE interfaces.

We find that the ability to resolve the grain boundary contribution from the low-frequency polarization tail depends strongly on the conformity of the CC|interlayer|SE contact. If the contact is non-conformal, as determined from pristine FIB-SEM cross-sections (Figure 3), an additional interface-related contribution can arise, which will be discussed below. This contribution can overlap with the polarization tail, resulting in the shift of the latter towards higher frequencies, thereby obscuring the grain boundary feature.[22,23,66]

EIS comparison of the pristine states of the different carbonaceous interlayers suggest that the HC-based interlayers exhibit poor interfacial contact (in accord with the cross-sections shown in Figure 3a,b), as no distinct grain-boundary contribution could be resolved and the polarization tail dominates the impedance spectra (Figure 5a,b, left panels). This behavior is consistent with the limited physical adhesion of these electrodes with only few contact points present between SE and interlayer. As a result, they tended to delaminate from the SE, even after isostatic pressing at high pressures. In contrast, the finer CB-based interlayers display a more distinctly separated grain boundary feature of the NZSP, although the overall response still deviates from ideal case of a fully separated semicircle, with the finer CB_f exhibiting the most pronounced separation (Figure 5c,d, left panels). This suggests that a smaller particle size in the carbon layer promotes a larger number of microcontact spots, a greater effective contact area, and thus a more intimate interlayer|SE interface as supported by cross-sections of the pristine cells.

Upon cathodic electrodeposition, the current was interrupted ($dQ_A = 75$ μAh·cm^{-2}) to record the impedance of the cell and thereby infer the evolution of the morphology and the interfacial characteristics of the electrodeposited sodium. Going from the pristine state to electrodeposition, the half-cells transition from a blocking to a non-blocking electrode configuration, evidencing the onset of sodium metal deposition at the WE (Figure 5a–d, right panels). A depressed semicircle owes to the overlap of multiple contributions, introducing an additional interface-related contribution (f_{apex} ~ 200−300 kHz).[67]

We have previously shown that this additional contribution is governed by dynamic current constriction,[22,23,66] as sodium deposition proceeds non-uniformly both laterally and vertically, leading to the formation of metal islands, whiskers, and interfacial gaps.[16] At high frequencies, these gaps behave as dielectrically conductive pathways. At low frequencies, however, they act as current-blocking regions, which manifests as a distinct feature in the impedance spectra and reflects the morphology of the electrochemically active contact area, including the distribution and the depth of interfacial gaps.[22,23,66] A detailed discussion of the impedance evolution for HC and CB carbons is presented below.

Furthermore, all impedance spectra exhibited an increase in impedance at low frequencies ($f < 5$ kHz) after initial electrodeposition, which has also been seen for other reservoir-free sodium systems and commonly attributed to diffusion processes.[16,67,68] While a detailed analysis of this contribution lies beyond the scope of the present study, it can nevertheless be concluded that this low frequency feature becomes more pronounced with decreasing particle size of the employed carbon interlayer material.

HC-Based Interlayers during Electrodeposition. As mentioned above, the spectra tracking the impedance evolution during cathode deposition for cells employing HC interlayers are characterized by a strong overlap of contributions originating from the SE and the interface-related processes. Owing to the concurrent evolution and strong overlap of these processes, reliable boundary conditions cannot be defined and thus prevent meaningful quantitative fitting of the spectra. Consequently, the following discussion is restricted to a qualitative evaluation.

Upon electrodeposition, a progressive shift of the spectra toward lower impedance values is observed in the high-frequency region (f ~ 1−7 MHz; Figure 5a,b, right panels). This shift reflects a change in the effective cell constant and manifests as a reduction of both the bulk and grain

https://doi.org/10.1021/acselectrochem.6c00121
ACS Electrochem. 2026, 2, 1887−1903

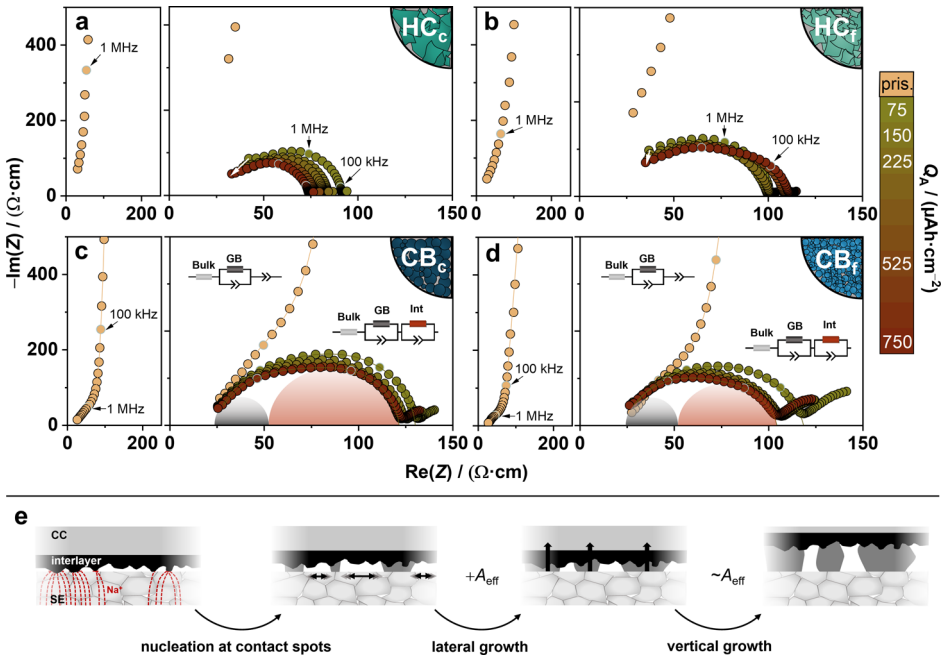

Figure 5. Impedance evolution in Nyquist plot presentation recorded with potentiostatic impedance spectroscopy (7 MHz–100 Hz) of half-cells with carbonaceous interlayers during cathodic deposition of 750 µAh·cm^{-2} sodium metal at 0.3 mA·cm^{-2} with an applied stack pressure of 1.5 MPa. Impedance was recorded in the pristine state (beige markers) and after every 75 µAh·cm^{-2} and a selected choice highlighted by the respective areal capacity is shown during electrodeposition for HC-based (a, b) and CB-based interlayers (c, d). Impedance evolution for CB-based interlayers was fitted with an equivalent circuit model with *R-RP-P* circuit for the pristine state and *R-RP-RP* for electrodeposited half-cells with nonblocking cell configuration, where *R* is the resistance and *P* refers to a constant phase element. (e) Schematic presentation of the proposed sodium nucleation and growth mechanism for CB-based interlayers derived from the impedance evolution.

boundary-related SE contributions, which are intrinsically coupled. This can arise from two concurrent effects. First, dendrite formation and propagation within the SE effectively reduce the ionic transport length through the SE, leading to a shift of the high-frequency response toward lower impedance. Second, the formation of a three-dimensional sodium electrode network through either infiltration of interstitial voids within the interlayer or dendritic sodium structures in the SE that increase the effective contact area. This expanding three-dimensional network further reduces the measured impedance.

These effects are markedly more pronounced for the coarse-structured HC$_c$-based interlayer. In HC$_c$-based cells, neither a distinct interface-related feature in the Nyquist representation (Figure 5a, right panel) nor a resolvable interface-related peak in the distribution of relaxation times (DRT) analysis was observed upon electrodeposition (Figure S11a), which is atypical for such systems.[16,20,31] Simulations have shown that once a critical effective contact area is exceeded, constriction-related contributions can no longer be resolved by impedance spectroscopy.[23] This provides a plausible explanation for the absence of an interface-related contribution in HC$_c$-based cells, where localized sodium deposition and infiltration into interstitial voids lead to the formation of an extended three-dimensional sodium network as evidenced by cross-sectional imaging analyses (Figure 3a).

In contrast, cells employing the finer HC$_f$-based interlayer exhibit a gradual increase in total cell impedance with ongoing electrodeposition (Figure 5b, right panel). While the SE-related impedance slightly decreases, consistent with dendrite formation, the interface-related contribution increases over time, indicating a progressive loss of effective interfacial contact area. Cross-sectional analyses revealed pronounced interfacial gaps between the deposited sodium and the HC$_f$ interlayer, while no infiltration of sodium into interstitial voids or formation of a three-dimensional sodium network were observed. The impedance increase can therefore be directly linked to contact loss at an effectively two-dimensional interface, which may be further promoted by a partially sodiophobic surface character of the HC$_f$-based interlayer.

Overall, the impedance evolution and cross-sectional analyses indicate that HC-based interlayers pose significant challenges for controlling sodium electrodeposition at the SE interface. In coarse HC$_c$ interlayers, sodium deposition proceeds via dendrite formation and infiltration into interstitial voids, leading to the development of an extended three-dimensional sodium network rather than film-like deposits. In contrast, finer HC$_f$ interlayers maintain an effectively two-dimensional interface but suffer from progressive contact loss, manifested by interfacial gap formation and a continuous increase in interfacial impedance. These distinct failure modes demonstrate that HC-based interlayers do not provide a stable or well-defined interfacial geometry.

CB-Based Interlayers during Electrodeposition. Both CB-based interlayers exhibit a similar trend in impedance evolution during electrodeposition, while the effects are more pronounced for the fine-particle CB$_f$ as shown in Figure 5c,d. Unlike for HC-based half-cells, the high-frequency region of the spectra remains largely unchanged, suggesting the absence of dendrite formation and propagation within the resolution of impedance spectroscopy. Furthermore, the overall cell

https://doi.org/10.1021/acselectrochem.6c00121
ACS Electrochem. 2026, 2, 1887−1903

impedance decreases markedly during the first electrodeposition step (75 μAh·cm^{-2}) and then remains nearly constant upon further deposition. This change can be attributed to the reduction of the interface-related contribution as the bulk and grain boundary contributions remain unchanged. This is further supported by fitting with an equivalent circuit model (Figure S12), as reliable boundary conditions can be defined in this case. The more pronounced initial resistance decrease for CB_f compared to CB_c points to a faster improvement of the interfacial contact. Overall, both CB-based interlayers exhibit an impedance evolution comparable to sodium electrodeposition at thermally evaporated copper electrodes, while offering a cost-effective and scalable alternative for solid-state RFCs.[16]

The impedance response provides mechanistic insight into the sodium growth process at CB-based interfaces (Figure 5e). During the early stages of electrodeposition, up to approximately 150 μAh·cm^{-2}, the sharp decrease in interface-related resistance indicates a rapid increase in effective contact area (A_{eff}). This points to predominantly lateral growth of the early sodium deposits at the interlayer|SE interface, facilitated by the low stack pressure, the low yield strength ($\sigma_y \sim 0.2$ MPa) and high homologous temperature of sodium ($T_h = T/T_m \sim 0.8$), which promote creep-mediated deformation and allows newly formed deposits to expand laterally.[61,62] Beyond 150 μAh·cm^{-2}, the interface-related resistance remains essentially unchanged, suggesting stagnation of the improvement of the interfacial effective contact area. In this regime, sodium deposition therefore transitions toward vertical growth. This behavior parallels observations in lithium-analogous systems, where initial nucleation site distribution governs subsequent metal growth and thereby determines overall electrode coverage.[60]

Optimization of the Interfacial Contact through Mechanical Interlocking

A conformal interface between the interlayer and the SE is crucial for establishing a well-defined contact geometry in the pristine state and for preventing delamination of the CC in regions adjacent to sodium deposits during electrodeposition. The strength and stability of these interfacial interactions are governed by the fundamental principle of adhesion. One pathway to enhance adhesion at solid-solid interfaces is the formation of material bridges formed through, e.g., mechanical interlocking.[69−71] The model proposed by McBain and Hopkins refers to the penetration and accommodation of surface asperities and voids of one material by a mechanically compliant counterpart, enabling the two surfaces to physically interlock and form key-keyway connections (Figure 6a).[72] Importantly, mechanical interlocking is not solely achieved by increasing the surface roughness, but it depends on the compatibility between the roughness features of the substrate and adhesive, as well as their mechanical properties, i.e., the ability of a softer material to conform to the topography of a harder material. Such interlocking increases the effective surface area, thereby strengthening the contribution of adhesion forces such as van der Waals and electrostatic interactions, and additionally redirects crack propagation along a tortuous and energy-dissipative path upon joint failure.[71] It was proposed that the combined contribution of mechanical interlocking and thermodynamic interfacial interactions can be expressed as a multiplicative relationship to estimate the joint strength G:[71]

$$G = (\text{constant}) \times (\text{mechanical keying component}) \times (\text{interfacial interactions component}) \quad (1)$$

Together, these effects define the initial interfacial conformity and influence the tendency for delamination of the carbon-coated CC in adjacent regions during electrodeposition between the carbonaceous interlayer ("adhesive") and the SE ("substrate").[20,73] To tailor these effects and optimize the interfacial contact mediated by the carbonaceous interlayer, we deliberately introduced surface roughness by employing an unpolished SE in half-cells.[74] Confocal microscopy highlights the pronounced difference in surface roughness between the polished and unpolished SE surfaces (Figure 6b,c). The P1000-polished SE exhibits characteristic polishing scratches but an overall lower roughness, with an arithmetical mean height Sa = (99 ± 10) nm. In contrast, the unpolished SE shows a substantially rougher topography with Sa = (196 ± 14) nm, accompanied by taller asperities, deeper valleys, and a significantly larger height range of up to 1.6 μm. These differences in surface topography directly influence the potential for mechanical interlocking together with a compliant interlayer to conform to the SE surface as demonstrated by peel strength measurements (Figure S13). Using an even finer polished SE surface (≥ P2500), on the other hand, prevented half-cell assembly, as the carbon-coated CC detached immediately after pressing and repeatedly fell off. Since no stable contact could be formed, measurements were not possible, underscoring that sufficient SE surface roughness is essential for interface adhesion.

We note that interfaces between NaSICON-type SEs and carbonaceous interlayers are governed by a complex interplay of factors, i.e., carbon micro- and mesostructure, void distribution, binder content, lamination pressure, and SE surface properties. These parameters determine the quality of interfacial contact in the pristine state. Interfacial adhesion, described by work of adhesion or interfacial toughness, integrates these effects and defines the initial conditions for homogeneous, layer-by-layer sodium electrodeposition through uniform current distribution.

This approach of increasing the surface roughness of the SE should be particularly effective for the fine CB_f-based interlayer as its enhanced deformability allows it to accommodate and fill the roughness features of the rigid SE, thereby improving adhesion through mechanical interlocking. Notably, peel strength measurements with varying PVDF to carbon ratios (Figure S13b) indicate that the carbon framework is the dominant contributor to interfacial adhesion. While PVDF is required for film formation, it does not dominate adhesion. Instead, adhesion is governed by particle-mediated mechanical interlocking within the carbon network, which also provides electronic conductivity and preserves a structurally accessible interface.

The potential profiles of half-cells with a CB_f-based interlayer displayed in Figure 7a reveal that the unpolished SE exhibits a markedly reduced nucleation overpotential ($\eta_{nuc} \sim 12$ mV) and growth overpotential ($\eta_{growth} \sim 7$ mV), consistent with a larger effective interfacial contact area, i.e., a larger number of electrochemically active nucleation sites in the initial stage of deposition and hence a larger area of sodium deposits covering the electrode area. The inset in Figure 7a highlights the characteristic sloping nucleation region prior to nucleation up to approximately 2 μAh·cm^{-2}. This resembles the early storage

https://doi.org/10.1021/acselectrochem.6c00121
ACS Electrochem. 2026, 2, 1887−1903

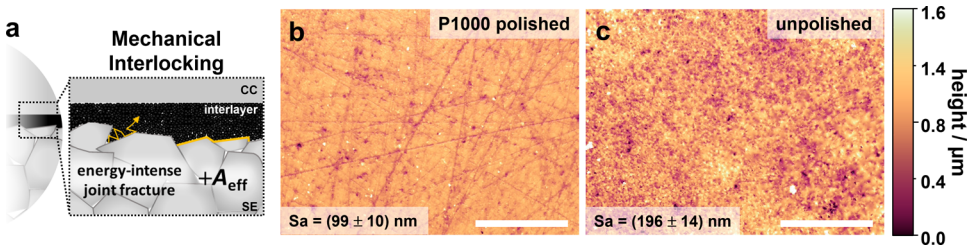

Figure 6. (a) Schematic illustration of the mechanical interlocking model proposed by McBain and Hopkins, as applied to the investigated carbonaceous RFC configuration. (b, c) Contour plots of a polished (P1000) and an unpolished solid electrolyte surface obtained by confocal microscopy, together with their corresponding arithmetical mean heights Sa. Scale bars represent 100 µm.

behavior reported for carbon frameworks in solid-state batteries and SIBs often associated with sodium accommodation through adsorption on defects and edges.[75]

The similarity suggests that improved interfacial conformity established through enhanced physical contact and stronger adhesion promotes a more homogeneous distribution of current across the interface. Such homogenization suppresses local current hotspots and enables initial sodium accommodation in the carbonaceous interlayer, as reflected in the potential profile. In contrast, the polished SE displays immediate electrodeposition, which is attributed to its limited interfacial kinetics and correspondingly higher local current densities (Figure S14a).[9] Thus, only the unpolished SE supports a brief insertion process prior to the onset of metal plating. The markedly reduced nucleation overpotential observed for the unpolished SE suggests that the interlayer acts as an effective "seed layer," lowering the nucleation barrier and facilitating sodium nucleation.[54,55] However, this behavior may also arise from the increased effective interfacial contact area. Consequently, the specific contribution of the interlayer to facilitating nucleation beyond improving the mechanical and electronic interface remains ambiguous and requires further investigation beyond the scope of this study.

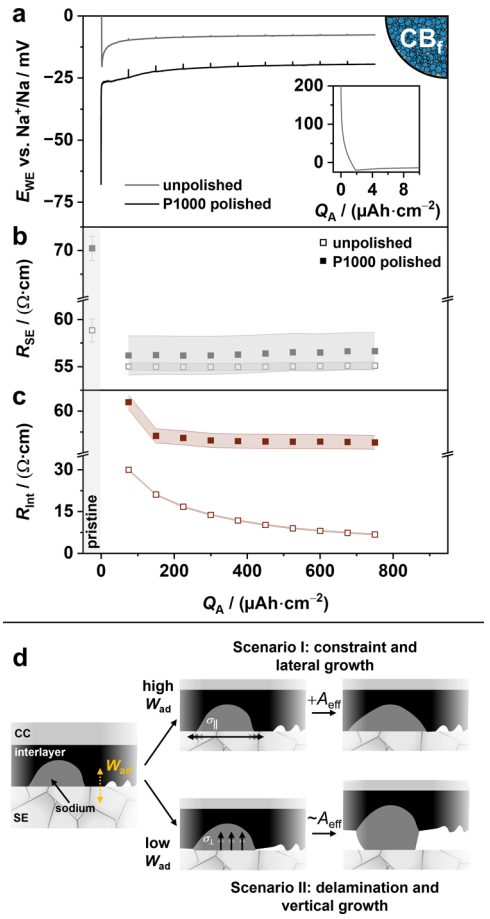

Figure 7. (a) Potential profiles of half-cells recorded during cathodic sodium deposition at a current density of 0.3 mA·cm^{-2} under an applied stack pressure of 1.5 MPa up to 750 µAh·cm^{-2} for cells with an unpolished and a polished SE surface in contact with a CB_f-based interlayer. (b) Evolution of the SE resistance obtained from fitting of the impedance spectra using an equivalent circuit model, comprising both bulk and grain boundary contributions of the SE. (c) Evolution of the interface-related resistance extracted from the same fits. Note that the error bars of the unpolished SE half-cell are smaller than the symbol size and therefore appear as a continuous line. (d) Schematic illustration of how interfacial adhesion governs sodium growth at the interlayer|SE interface.

Impedance analysis provides further evidence for the differing interface morphology between the polished and unpolished SE pellets. In the pristine state, the unpolished SE exhibits a more clearly resolved grain boundary contribution. It is visible as a more distinctly separated semicircle from the linear increase in impedance at low frequencies consistent with a more intimate interlayer|SE contact and thus stronger adhesion enabled by mechanical interlocking (Figure S14b). Upon fitting the spectra with an equivalent circuit model, an apparent decrease in the extracted SE resistance is observed between the pristine state and upon the first electrodeposition step for the SE (Figure 7b). This shift is not solely an artefact of the change in the equivalent circuit model, because this effect is minimal for the unpolished SE. This indicates that the higher resistance in the polished case arises mainly from an unresolved superposition of grain boundary and interface-related contributions, which artificially inflates the apparent SE resistance.

During electrodeposition, the SE resistance remains essentially unchanged for both samples, indicating that the electrolyte is unaffected and that dendrite formation and internal cracking are negligible as observed by impedance spectroscopy. In contrast, the interfacial resistance exhibits a markedly different evolution depending on the SE surface condition (Figure 7c). For the polished pellet, the interface-related contribution decreases only during the first two deposition steps and then remains constant, indicating that interfacial improvement is largely confined to the early stages of electrodeposition. Once the initial interfacial arrangement of sodium deposits has formed after approximately 150 µAh·cm^{-2}, further enhancement of the contact area appears limited. The unpolished pellet, however, shows a continuous

https://doi.org/10.1021/acselectrochem.6c00121
ACS Electrochem. 2026, 2, 1887−1903

and substantially stronger decrease in interfacial resistance. This pronounced reduction suggests a progressively increasing effective contact area as sodium deposits grow laterally.

We assume that strong interfacial adhesion not only suppresses early-stage delamination but also governs the growth mode of the plated sodium, as schematically illustrated in Figure 7d. When the carbon-coated CC|SE interface remains mechanically intact, the deposited metal becomes laterally constrained by the surrounding adhered regions. As established by chemo-mechanical models of interfacial debonding and blister suppression, such constraint generates in-plane compressive stresses within the growing metal layer, which promote lateral plastic flow rather than vertical separation.[60] The resulting stressed state is mechanically equivalent to an additional effective stack pressure and favors laterally extended growth, consistent with *operando* observations of confined lithium deformation during electrodeposition.[60,76] This situation is depicted in scenario I in Figure 7d by the laterally constrained sodium deposit and the in-plane stress component $\sigma_{\parallel}$.

In contrast, if interfacial adhesion is progressively weakened by stresses generated during sodium growth, local delamination of the carbon-coated CC from the SE can occur, representing interfacial joint failure, as in the case of the polished SE.[36,77] These mechanically decoupled sodium whiskers and islands then experience concentrated current and reduced lateral constraint, such that metal growth proceeds predominantly normal to the interface as vertically elongated deposits or filaments as seen in scenario II (Figure 7d).[78] In the schematic, this transition is reflected by the formation of interfacial gaps, the loss of lateral constraint, and the dominance of out-of-plane stress $\sigma_{\perp}$. Thus, the rough surface topography of the unpolished SE prevents delamination of the carbon-coated CC, enabling mechanical interlocking and thereby supporting the horizontal expansion of the sodium layer, which in turn establishes a more continuous and stable interfacial contact throughout early stages of electrodeposition.

In summary, sodium nucleation and growth in RFCs with a NaSICON-type SE is dictated by the initial contact geometry at the interface of CC and SE. This critical interaction in adhesion between CC and the SE can be tailored through the following strategies:

i) Employing a thin, low-cost carbonaceous interlayer as an electronic and mechanical contact mediator, effectively enabling electron transport and mechanical buffering directly at the interface.

ii) Optimizing the mesoscale deformability and contact formation of the interlayer by using small primary carbon particles, which (a) increase the number of microcontact points, (b) allow local rearrangement and mechanical compliance under low stack pressure and electrodeposition-induced stresses generated at the interface, and (c) thereby establish a more continuous and conformal effective interfacial contact area.

iii) Enhancing mechanical engagement at the SE surface by tuning SE topography, where increased surface roughness provides accessible asperities and voids that the compliant carbon network can accommodate, increasing the adhesion through mechanical interlocking.

Together, these interfacial design principles provide a framework for directing sodium electrodeposition toward laterally extended growth, enabling low-cost and efficient operation of sodium-based solid-state RFCs.

CONCLUSIONS

This work demonstrates that the mesoscale particle architecture of non-graphitic carbon interlayers, specifically particle size (23–1200 nm) and compactability, critically determines interfacial contact formation, sodium deposition morphology, and dendrite propensity in reservoir-free sodium solid-state cells with a NaSICON-type SE. Coarse particles provide fewer contact points and a smaller effective contact area, resulting in current focusing and accelerated dendritic growth, most notably for HC-based interlayers. In all systems, sodium deposits as islands and whiskers at the interlayer|SE interface, consistent with the electronic and adhesional properties of the carbon interlayers. Among the evaluated materials, a fine CB_f-based interlayer (average particle size ~ 23 nm) enables the most homogeneous electrodeposition. Its high deformability and adhesion toward the SE allow it to function as a mechanically adaptive "cushion", establishing intimate interfacial contact and stabilizing the CC|interlayer|SE interface.

The study further highlights that strong adhesion is key to establish a stable initial interface, suppressing delamination, and promoting extended lateral sodium growth. Increasing the mechanical interlocking component between the fine CB interlayer and an unpolished, rough SE surface stabilizes early deposition, while a sloping regime in the potential profile indicates sodium insertion presumably facilitating nucleation. Together, these results link carbon microstructure, SE topography, and interfacial mechanics to the nucleation and growth behavior of sodium metal.

Building on these results, high-resolution transmission electron microscopy (TEM) or scanning transmission electron microscopy coupled with energy-dispersive X-ray spectroscopy (STEM-EDS) analyses will be required to determine whether the sodium detected within the CB_f-based interlayer resides in interstitial voids or is inserted into the carbon particles themselves, thereby clarifying the nanoscale sodium distribution. This distinction is important, as partial sodiation of the carbon could act as a "seed layer" and potentially facilitate nucleation. In addition, systematic deposition–dissolution studies are needed to assess the reversibility of this sodium insertion and to determine whether any sodium remains trapped within the carbonaceous interlayer upon cycling. Taken together, this work highlights the interconnected roles of mechanical deformability of the interlayer, interfacial adhesion, and SE surface topography at the carbonaceous interlayer|NZSP interface. Their coordinated optimization emerges as a key requirement for achieving stable and uniform sodium deposition in sodium RFCs and provides a foundation for future interlayer design with NaSICON-type SEs.

EXPERIMENTAL SECTION

Synthesis of the Solid Electrolyte

All NaSICON-type SE pellets reported herein with $Na_{3.4}Zr_2Si_{2.4}P_{0.6}O_{12}$·1.5 at % Na_3PO_4 were synthesized by a modified solution-assisted solid-state reaction reported by Ma et al.[65] The SE, NZSP, was prepared in 3 g batches by first dissolving stoichiometric amounts of $ZrO(NO_3)_2 \cdot x\ H_2O$ (x = 6 by thermal analysis; 99%, *Sigma Aldrich*) in approximately 50 mL deionized water. The precursor was hand ground in an agate mortar in prior. After stirring overnight at room temperature, $NaNO_3$ (99%, *Sigma Aldrich*), nitric acid (70%, *Sigma Aldrich*), and $Si(OCH_2CH_3)_4$ (98%, *Merck*) were added in the given order thus forming a biphasic mixture and hydrolyzing

https://doi.org/10.1021/acselectrochem.6c00121
ACS Electrochem. 2026, 2, 1887−1903

after stirring overnight. After addition of $NH_4H_2PO_4$ (99%, *Acros Organics*), a colorless precipitate was received. To remove the solvent, the material was heated to 85 °C in a sand bath, after which the resulting white solid was stored in an oven at 80 °C. The mixture was transferred to an alumina crucible and calcined at 800 °C for 3 h with a heating and cooling rate of 180 °C·h^{-1} in a muffle furnace (*L 5/13/P330*) by *Nabertherm*. The white solid was ball milled with zirconia balls (d = 5 mm) and ethanol at a weight ratio of 1:10:1 in a *Pulverisette 7* by *Fritsch* in zirconia cups (180 rpm for 15 min, 10 min rest, 80 cycles). Afterwards, the obtained crude product was dried in an oven at 60 °C followed by *in vacuo* drying in a *Büchi* glass oven at 80 °C overnight. Pellets were prepared by transferring 500 mg or 250 mg into a cylindrical pressing mold with a diameter of 13 mm or 10 mm, which were pressed uniaxially at 220 MPa for 3 min or under an applied torque of 10 Nm for 2 min. The pellets were covered with mother powder, placed on platinum foil, and sintered at 1285 °C for 5 h with a heating and cooling rate of 180 °C·h^{-1} in a high-temperature furnace (*HT04/17*) by *Nabertherm* yielding pellets with 11 mm or 8 mm diameter and approximately 1.6 mm thickness. The relative density of the SE was determined geometrically, assuming a cylindrical shape, and was found to be ≥ 90%. It needs to be noted that upscaling of the synthesis (5 g) led to the formation of a glassy phase upon sintering.

Synthesis of the Hard Carbon

The synthesis of resorcinol-formaldehyde-derived HC powder was based on the procedure reported by Tanaka et al. and modified as follows: resorcinol (551 mg, 99%, *Sigma Aldrich*) was dissolved in deionized water (1.45 mL) by stirring at room temperature for 10 min in a glass vial.[79] 5 M hydrochloric acid (50 μL), which was prepared previously upon mixing deionized water (2.917 mL) with fuming hydrochloric acid (2.083 mL, 37%, *VWR Chemicals*), were added. Afterwards, absolute ethanol (4.835 mL, 99.8%, *Fisher Chemicals*) as well as triethyl orthoacetate (456 μL, 97%, *Thermo Scientific*) and 37 wt % aqueous formaldehyde solutions (550 μL, stab. 10–15% methanol, *Sigma Aldrich*) were added one after another. The clear solution was stirred at 30 °C for 30 min before cross-linking. Thermopolymerization between resorcinol and the aldehyde species was initiated upon a thermal treatment at 80 °C over night. A hard brown solid was obtained, which was scratched out of the glass vial and transferred into a crucible for carbonization in a tube furnace (*STF 16/18* from *Carbolite Gero Ltd.*) in nitrogen atmosphere (N_2 flow rate of 500 mL min^{-1}, heating rate of 1 K min^{-1} with 1 h dwelling time at 400 °C and 2 h dwelling time at 900 °C, cooling with 4 K min^{-1}). The black product was hand-mortared for 6 h in order to obtain the coarse HC powder HC_c.

The particles size for the finer HC_f was further reduced by ball-milling. A 1 h hand-mortared non-templated resorcinol-formaldehyde-derived HC derived by the same route as for HC_c was subsequently used in a ball-milling step with zirconia balls (d = 5 mm) at a weight ratio of 1:40 in a *Pulverisette 7* by *Fritsch* (500 rpm for 10 min, 5 min rest, 12 cycles) in zirconia cups.

Material Characterization

X-ray Scattering. The phase purity of the SE for each synthesized batch was investigated *via* powder X-ray diffraction (XRD) analysis, which was performed on *Empyrean Series 2* by *PANanalytic* in Bragg-Brentano geometry with a monochromatic Cu-K_α-X-ray beam with wavelengths of λ_1 = 154.06 pm ($K_{\alpha1}$) and λ_2 = 154.44 pm ($K_{\alpha2}$). The hand-ground sintered pellet was mounted on a (911)-oriented silicon single crystal sample holder. All measurements were carried out at an operating voltage of 40 V and a current of 40 mA. The following measurement range of 2θ = 10°–70° was used with a step size of 0.013° and a measurement time of 150 s per step. The obtained XRD data were analyzed with *HighScore*.

Wide-Angle X-ray Scattering for Carbon Nanoscale Microstructural Analysis. Wide-angle X-ray scattering (WAXS) was carried out for the examination of the carbon microstructure, i.e., the graphene layers' arrangement, dimensions, and stacking. A *XRDynamic 500* diffractometer from *Anton Paar* was used in Bragg-Brentano geometry at room temperature with Cu-$K_{\alpha1}$ radiation (λ = 1.5406 Å) and Cu-$K_{\alpha2}$ radiation (λ = 1.5444 Å) in a 1:2 ratio. The operating voltage was 40 kV with a current of 50 mA. Within the measurement range of 2θ = 10°–115° a step size of 0.1° and measurement time per step of 900 s was applied. To obtain quantitative microstructural information, the algorithm of Ruland and Smarsly was used.[46] Implemented in the *OctCarb* script by Osswald and Smarsly,[80] it was executed by the GNU *Octave* software to fit the whole experimental WAXS data curve with a theoretical model function while minimizing the deviation to the experimental data. Detailed information about mathematical basis of the algorithm and the calculation of physical and geometrical parameters describing the carbon microstructure are out of the scope of this article and can be found in previous publications.[46,81,82]

Electronic Conductivity Measurements. The electronic conductivity of the carbon materials was measured in four-point geometry following the procedure by Sánchez-González et al. (Scheme 1).[49] Two steel pistons (d = 2 mm) were used to apply the current and define the cross-sectional area A, while the two copper wires (d = 1 mm) inserted into the polyether ether ketone (PEEK) inlet at a defined separation L, served as potential probes, where L corresponds to the distance between the two voltage-sensing contacts. The resistance R was recorded with a digital multimeter (*Keithley 2007*) operated with the 4-wire resistance function (Ω4 mode). The carbon powders were gradually filled into the cylindrical column and continually compacted under the designated pressure using an in-house-built pressing apparatus.[51] The conductivity was then determined by $\sigma_{el} = \frac{L}{A \cdot R}$. All measurements were conducted three times at the designated pressure.

Peel Strength Measurements. Peel tests were conducted to quantify the interfacial toughness of carbonaceous interlayers on SE substrates using a geometry adapted from Liao and co-workers.[37] The interlayers were pressed onto the SE under conditions identical to those used for half-cells and subsequently peeled off under controlled conditions. The interfacial toughness Γ was calculated according to

$$\Gamma = \frac{2F}{b} \tag{2}$$

where F is the applied force and b = 6 mm is the effective contact width. No force correction was applied, as no permanent curling of the tape was observed. Thus, the applied weight was directly approximated and converted into the acting force with 2–3 measurements per tested combination. Errors were approximated with error propagation assuming an error of 0.5 mm as Δb. Further details are provided in the Supporting Information (Figure S13).

Scheme 1. Pressure-Dependent Four-Point Measurement Setup for Electronic Conductivity Measurements of the Carbon Interlayer Materials with Stainless Steel Pistons Closing the Current Circuit and Copper Wires for Determination of the Potential

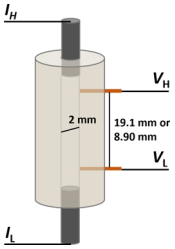

https://doi.org/10.1021/acselectrochem.6c00121
ACS Electrochem. 2026, 2, 1887–1903

Scanning Electron Microscopy. Morphology of the SE and carbon films was investigated by means of SEM using the high-resolution field-emission SEM instrument *GeminiSEM 560* by *Zeiss*. Detection of secondary electrons was performed with the detectors *SE2* and *Inlens*, which were operated at either 2.0 kV with a 20 μm probe aperture or 5.0 kV with a 15 μm probe aperture in imaging mode. SEM images were analyzed with *ImageJ*.

3D Confocal Microscopy. Roughness analyses of the SE topography of an unpolished and P1000 polished SE was investigated by means of confocal microscopy using a *S Neox* confocal microscope by *Sensofar* with an *EPI 50x PLANAPO* objective together with the *SensoSCAN 6.7* software package. An area of 350.88 × 264.19 μm^2 was scanned with a pixel size of 0.26 μm/pixel using a green LED (light intensity ∼ 1.3%). Data were processed and evaluated using *SensoVIEW 2.6.0*. The measured 3D profiles were leveled with the 'plane' function for comparability. Missing data points were reconstructed by interpolation with a bicubic function.

Cell Preparation

All work with chemicals, which were dried *in vacuo* in a *Büchi* glass oven beforehand, was conducted in an Ar-filled glove-box by *MBraun* ($p(O_2)/p < 5$ ppm, $p(H_2O)/p < 5$ ppm).

Preparation of Carbon Tapes. Carbon tapes were prepared in the following order: SuperPLi conductive carbon (*TimCal*, average particle size (APS) according to supplier ∼ 40 nm) or carbon black FW 200 (*Degussa*, APS according to supplier ∼ 13 nm) and PVDF (5 wt % in NMP) were dispersed in *N*-methyl-2-pyrrolidone (NMP) in a polymer cup. Three zirconia balls (d = 5 mm) were added to the suspension and the mixture was ball milled in a speed mixer at 2000 rpm for 1 min. NMP was added gradually with mixing steps in between and finally mixed at 2000 rpm for 5 min until a uniform slurry was formed. The slurry exhibits a weight ratio of 93:7, 85:15, and 80:20 referring to carbon:PVDF at a solid weight content of ∼ 5–10%. The obtained slurry was cast rapidly (5 $mm \cdot s^{-1}$) onto aluminum foil (∼ 17 μm) at a thickness of 30 μm at 60 °C, followed by drying at 80 °C *in vacuo* for 12 h, and punching circular disks (d = 5 mm), which serve as WE in the following process. Interlayers for HC_f and CB_c had to be retaped for EDS measurements as the glovebox atmosphere contaminates the surface over extended storage times thereby changing the electrodeposition behavior. The solid weight content was slightly lower for the retaped HC_f-interlayer explaining the difference in thickness.

Preparation of Metal Electrodes for Solid Electrolyte Conductivity Determination. For determination of the ionic conductivity of the SE, symmetric cells with gold blocking electrodes were prepared (Au|SE|Au). A NaSICON pellet (d = 8 mm) was first polished with grit P1500 SiC-paper and covered with gold layers with a thickness of 150 nm by thermal evaporation on both sides ($d_{aperture}$ = 6 mm).

Cell Assembly. Cells reported herein were fabricated as half-cells with the following configuration unless otherwise noted: Al|interlayer|SE|Na_{id}|Cu. As a CE, a sodium electrode is used that meets the requirements of a quasi-reference electrode (Na_{id}).[51] As the resistance of the Na|NaSICON interface has been found to be negligibly small (∼ 1 $\Omega \cdot cm^2$) following an isostatic pressing procedure of the sodium electrode onto the SE, this electrode can be seen as an ideal CE.[52] Hence, Na_{id} acts as combined CE and RE as long as no interfacial contribution arises from sodium dissolution, which was monitored through polarization due to pore formation at the CE in the potential profile during cathodic deposition. No such polarization was observed, and we therefore assume negligible contribution of the CE. Therefore, any changes observed during the electrochemical measurements of the cells are ascribed to the WE at used areal capacity of 750 $\mu Ah \cdot cm^{-2}$.[51] These sodium CEs (*BASF*) were prepared through repeated flattening with plastic wrap in a hand pressing apparatus and subsequent punching into circular disks (d = 6 mm). The sodium disks were placed on copper foil (d = 10 mm or 8 mm) and cleaned by scratching the surface with a ceramic knife before pressing onto the as-sintered pellet. For measurements with polished pellets, the NaSICON pellets were polished up to grit P1000 with SiC-paper on the side contacting the WE in the following (Scheme 2). The CE was attached by hand pressing and subsequent isostatic pressing. For this, the half-cells were sealed in pouch bags (4 cm × 4 cm) under vacuum and isostatically pressed in a slab press with an isostatic pressure chamber by *LOOMIS* at 100 MPa for 15 min. After removal of the pouch casings, the cells were contacted with nickel CCs (d = 4 mm, *MTI*), which were fixated with *Kapton* tape and sealed in pouch bags under vacuum (4 cm × 7 cm). A polished nickel disk (d = 12 mm; polished up to 1 μm diamond suspension) was placed in between the nickel CC tab and the WE to ensure sufficient contact and equal pressure distribution during sodium deposition. After electrochemical characterization, the plated WE was removed with *Kapton* tape, while retaining the CE. The pellet was reused by removal of all sodium residues through polishing up to grit P1000 followed by attaching of a new WE in the described manner displayed in Scheme 2.

Electrochemical Characterization

An additional external load of 1.5 MPa was applied by using an in-house-built pressing apparatus reported by Krauskopf et al. for plating experiments.[51] Electrochemical characterizations were carried out in a climate chamber by *Binder* at 25 °C using a *Biologic VMP 300* potentiostat (*BioLogic Sciences Instruments*). Arrhenius measurements were carried out inside a climate chamber by *Weiss Technik LabEvent* with a *SP 300* potentiostat. The obtained data were analyzed with *EC-Lab* (vers. 11). For potentiostatic electrochemical impedance spectroscopy (PEIS) measurements, an amplitude of 10 mV was applied within a frequency range between 7 MHz and 100 Hz to minimize the time for interruptions during electrodeposition and maintain the steady state criterium. For the first 1 h, the cells were equilibrated recording a PEIS spectrum every 30 min. After equilibration, the cells were plated by applying a current density of 0.3 $mA \cdot cm^{-2}$, while recoding the potential at a sampling rate of 10 Hz during the first step to resolve the nucleation overpotential. If not stated otherwise, plating steps were interrupted after 75 $\mu Ah \cdot cm^{-2}$ until 750 $\mu Ah \cdot cm^{-2}$ of sodium was deposited at the WE. Before and after each impedance measurement, the cell was allowed to equilibrate for 4 s in open circuit voltage (OCV) mode. All measurements were performed with two cells.

Scheme 2. General Assembly of Half-Cells with Polished SE

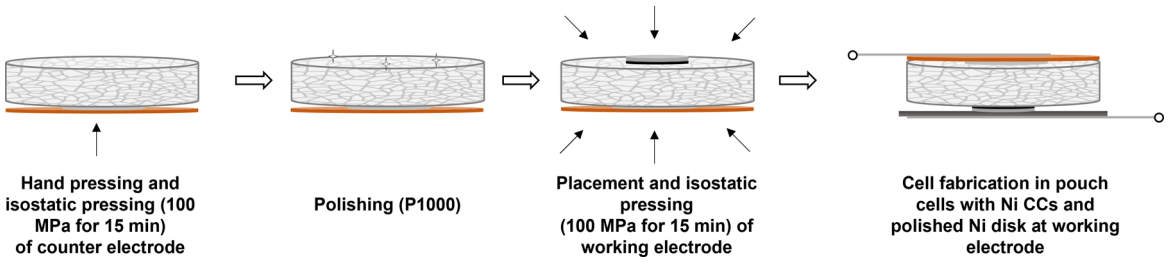

https://doi.org/10.1021/acselectrochem.6c00121
ACS Electrochem. 2026, 2, 1887−1903

Analysis of impedance data was conducted by fitting with an equivalent circuit model using *RelaxIS 3* (*rhd Instruments*, vers. 3), if possible. Data points in the higher and lower frequency range with a relative error greater than 5% in Kramers–Kronig test were excluded from fitting.[52] All PEIS data of half-cells were normalized by multiplication with the cell constant $\frac{A_{theo}}{L}$. The effective cell constant was determined using a theoretical geometric area of the electrode $A_{theo} = \frac{L}{\sigma_{bulk} \cdot R_{bulk}}$, where L is the SE thickness. An identical bulk resistance was assumed for all cells, consistent with bulk ionic conductivity measurements obtained from symmetric Au|SE|Au cells (σ_{bulk} = 0.145 S·cm^{-1}). For CB-based cells, the bulk resistance R_{bulk} was extracted directly from pristine-state fits based on pristine-state impedance spectra using an equivalent circuit of the form *R-RP-P*. The first resistance *R* represents the bulk SE contribution, while the second *RP* element corresponds to the SE grain boundary response. Furthermore, a constant phase element *P* accounts for the low-frequency polarization tail in the pristine state. For HC-based cells, where reliable separation of bulk, grain boundary, and polarization tail contributions was not possible, R_{bulk} was approximated by the real part of the impedance at the highest measured frequency (Re(Z) at 7 MHz). All SE- and interface-related resistances derived from fitting, as well as the real and imaginary components of the impedance (Re(Z), −Im(Z)), were also normalized by multiplication with the cell constant $\frac{A_{theo}}{L}$. This procedure was applied uniformly to all half-cells also after electrodeposition, while the ratio between bulk and grain boundary resistance was kept fixed based on the unpolished half-cell. For fitting, the equivalent circuit model was altered by replacing the constant phase element *P* by an *RP* element included for non-blocking cells to account for interface-related contributions. Distribution of relaxation times (DRT) analyses were performed with a Gaussian basis function, a second order derivative (shape factor: 0.5), and $\lambda = 10^{-3}$ within a frequency range between 5 MHz and 1 kHz, considering real and imaginary parts of the impedance, using the distribution function for regularization

Post Mortem Characterization

The plated cells were prepared for *ex situ* analysis by mounting the sample on an aluminum stub at 45° covered with an adhesive copper tape on a *Leica* stub and transferred with a *Leica VCT500* transfer module with cryo stage. Cross sections of half-cells with *in situ* electrodeposited sodium were prepared with a Xe plasma-focused-ion-beam scanning electron microscope (FIB-SEM) *XEIA3* by *Tescan* under cryogenic conditions (< −120 °C) at 30 kV with 370 nA beam current (400 µm probe aperture). Two polishing steps followed (112 nA, 400 µm or 100 nA, 400 µm and 32 nA, 200 µm or 15 nA, 200 µm). SEM imaging was conducted at 4 kV with the *SE* detector and a detector for low energy backscattered electrons (*LE-BSE*) in analytic or ultra-high resolution mode. SEM images were analyzed with *ImageJ*. Investigation of the atom distribution was performed by means of SEM using the high-resolution field-emission SEM instrument *GeminiSEM 560* by *Zeiss* with the EDS detector *Ultim Extreme* by *Oxford Instruments* at 5.0 kV with a 60 µm or 120 µm probe aperture at high current in imaging or normal mode under cryogenic conditions (< −80 °C). The obtained data were analyzed with *Aztec 3.2* utilizing a linear fit auto brightness with a binning factor of 1. Smoothing of element maps proceeded with a Gaussian function and binning of 3 × 3.

■ ASSOCIATED CONTENT

Data Availability Statement

The data that support the findings of this study are openly available at Zenodo at DOI: 10.5281/zenodo.18786491.

Supporting Information

The Supporting Information is available free of charge at https://pubs.acs.org/doi/10.1021/acselectrochem.6c00121.

Additional experimental details, methods, and measurements (DOCX)

■ AUTHOR INFORMATION

Corresponding Author

Jürgen Janek – *Institute of Physical Chemistry and Center for Materials Research (ZfM), Justus Liebig University, Heinrich-Buff-Ring 17, Giessen D-35392, Germany*; orcid.org/0000-0002-9221-4756; Email: juergen.janek@uni-giessen.de

Authors

Maya Ziegler – *Institute of Physical Chemistry and Center for Materials Research (ZfM), Justus Liebig University, Heinrich-Buff-Ring 17, Giessen D-35392, Germany*

Till Ortmann – *Institute of Physical Chemistry and Center for Materials Research (ZfM), Justus Liebig University, Heinrich-Buff-Ring 17, Giessen D-35392, Germany*; orcid.org/0000-0001-8482-1794

Chantal Glatthaar – *Institute of Physical Chemistry and Center for Materials Research (ZfM), Justus Liebig University, Heinrich-Buff-Ring 17, Giessen D-35392, Germany*; orcid.org/0009-0000-7413-5926

Jona-Matteo Werner – *Institute of Physical Chemistry and Center for Materials Research (ZfM), Justus Liebig University, Heinrich-Buff-Ring 17, Giessen D-35392, Germany*

Vipin K. Singh – *Department of Chemistry and the Waterloo Institute for Nanotechnology, University of Waterloo, Waterloo, Ontario N2L 3G1, Canada*

Boris Mogwitz – *Institute of Physical Chemistry and Center for Materials Research (ZfM), Justus Liebig University, Heinrich-Buff-Ring 17, Giessen D-35392, Germany*

Janis K. Eckhardt – *Institute of Physical Chemistry and Center for Materials Research (ZfM), Justus Liebig University, Heinrich-Buff-Ring 17, Giessen D-35392, Germany*; orcid.org/0000-0002-2799-0599

Bernd M. Smarsly – *Institute of Physical Chemistry and Center for Materials Research (ZfM), Justus Liebig University, Heinrich-Buff-Ring 17, Giessen D-35392, Germany*; orcid.org/0000-0001-8452-2663

Linda F. Nazar – *Department of Chemistry and the Waterloo Institute for Nanotechnology, University of Waterloo, Waterloo, Ontario N2L 3G1, Canada*; orcid.org/0000-0002-3314-8197

Marcus Rohnke – *Institute of Physical Chemistry and Center for Materials Research (ZfM), Justus Liebig University, Heinrich-Buff-Ring 17, Giessen D-35392, Germany*; orcid.org/0000-0002-8867-950X

Complete contact information is available at: https://pubs.acs.org/doi/10.1021/acselectrochem.6c00121

Notes

The authors declare no competing financial interest.

■ ACKNOWLEDGMENTS

M.Z. sincerely thanks Klaus Peppler for his guidance and introduction to SEM and EDS analyses and Till Fuchs for fruitful discussions. This work contributes to the research performed at CELEST (Center for Electrochemical Energy Storage Ulm-Karlsruhe) and was funded by the German Research

Foundation (DFG) under Project ID 390874152 (POLiS Cluster of Excellence). C.G. thanks the German Academic Scholarship Foundation for financial support as well as the joint graduate program between Schunk group and Justus Liebig University Giessen. L.F.N. and V.K.S. thank the Ontario Research Fund (ORF-RE) for financial support and NSERC for platform support through the Discovery Grant and Canada Research Chair program. The language and grammar of the manuscript have partially been improved with the help of ChatGPT (vers. 5.2, *OpenAI*).

■ REFERENCES

(1) Yao, A.; Benson, S. M.; Chueh, W. C. Critically assessing sodium-ion technology roadmaps and scenarios for techno-economic competitiveness against lithium-ion batteries. *Nat. Energy* **2025**, *10* (3), 404–416.
(2) Phogat, P.; Dey, S.; Wan, M. Comprehensive review of Sodium-Ion Batteries: Principles, Materials, Performance, Challenges, and future Perspectives. *Mater. Sci. Eng., B* **2025**, *312*, 117870.
(3) Stevens, D. A.; Dahn, J. R. High Capacity Anode Materials for Rechargeable Sodium-Ion Batteries. *J. Electrochem. Soc.* **2000**, *147* (4), 1271.
(4) Dou, X.; Hasa, I.; Saurel, D.; Vaalma, C.; Wu, L.; Buchholz, D.; Bresser, D.; Komaba, S.; Passerini, S. Hard carbons for sodium-ion batteries: Structure, analysis, sustainability, and electrochemistry. *Mater. Today* **2019**, *23*, 87–104.
(5) Wu, C.; Yang, Y.; Zhang, Y.; Xu, H.; He, X.; Wu, X.; Chou, S. Hard carbon for sodium-ion batteries: progress, strategies and future perspective. *Chem. Sci.* **2024**, *15* (17), 6244–6268.
(6) Díez, N.; Sevilla, M.; Fuertes, A. B. Synthesis strategies of templated porous carbons beyond the silica nanocasting technique. *Carbon* **2021**, *178*, 451–476.
(7) Zhou, H.; Song, Y.; Zhang, B.; Sun, H.; Khurshid, I. A.; Kong, Y.; Chen, L.; Cui, L.; Zhang, D.; Wang, W.; Yang, L.; Du, X. Overview of electrochemical competing process of sodium storage and metal plating in hard carbon anode of sodium ion battery. *Energy Storage Mater.* **2024**, *71*, 103645.
(8) Glatthaar, C.; Badaczewski, F.; Klar, P. J.; Smarsly, B. M. Between Order and Confusion: Clearing up Structural Misconceptions in Carbon Materials Nomenclature. *Angew. Chem., Int. Ed.* **2026**, *65* (11), e19975.
(9) Guo, Z.; Xu, Z.; Xie, F.; Jiang, J.; Zheng, K.; Alabidun, S.; Crespo-Ribadeneyra, M.; Hu, Y.-S.; Au, H.; Titirici, M.-M. Investigating the Superior Performance of Hard Carbon Anodes in Sodium-Ion Compared With Lithium- and Potassium-Ion Batteries. *Adv. Mater.* **2023**, *35* (42), e2304091.
(10) Schäfer, D.; Hankins, K.; Allion, M.; Krewer, U.; Karcher, F.; Derr, L.; Schuster, R.; Maibach, J.; Mück, S.; Kramer, D.; Mönig, R.; Jeschull, F.; Daboss, S.; Philipp, T.; Neusser, G.; Romer, J.; Palanisamy, K.; Kranz, C.; Buchner, F.; Behm, R. J.; Ahmadian, A.; Kübel, C.; Mohammad, I.; Samoson, A.; Witter, R.; Smarsly, B.; Rohnke, M. Multiscale Investigation of Sodium-Ion Battery Anodes: Analytical Techniques and Applications. *Adv. Energy Mater.* **2024**, *14* (15), 2302830.
(11) Fang, Z.; Smith, J.; Clelland, K.; Tseng, K.-T.; Wolfenstine, J.; Delaire, O.; Sakamoto, J.; Chi, M. Ionic conduction and interfacial stability in $Na_{1+x}Zr_2Si_xP_{3-x}O_{12}$ solid electrolytes: Past, present, and future perspectives. *Appl. Phys. Rev.* **2025**, *12* (1), 011329.
(12) Janek, J.; Zeier, W. G. Challenges in speeding up solid-state battery development. *Nat. Energy* **2023**, *8* (3), 230–240.
(13) Janek, J.; Zeier, W. G. A solid future for battery development. *Nat. Energy* **2016**, *1* (9), 16141.
(14) Deysher, G.; Oh, J. A. S.; Chen, Y.-T.; Sayahpour, B.; Ham, S.-Y.; Cheng, D.; Ridley, P.; Cronk, A.; Lin, S. W.-H.; Qian, K.; Nguyen, L. H. B.; Jang, J.; Meng, Y. S. Design principles for enabling an anode-free sodium all-solid-state battery. *Nat. Energy* **2024**, *9*, 1161–1172.
(15) Heubner, C.; Maletti, S.; Auer, H.; Hüttl, J.; Voigt, K.; Lohrberg, O.; Nikolowski, K.; Partsch, M.; Michaelis, A. From Lithium-Metal toward Anode-Free Solid-State Batteries: Current Developments, Issues, and Challenges. *Adv. Funct. Mater.* **2021**, *31* (51), 2106608.
(16) Ortmann, T.; Fuchs, T.; Eckhardt, J. K.; Ding, Z.; Ma, Q.; Tietz, F.; Kübel, C.; Rohnke, M.; Janek, J. Deposition of Sodium Metal at the Copper-NaSICON Interface for Reservoir-Free Solid-State Sodium Batteries. *Adv. Energy Mater.* **2024**, *14* (15), 2302729.
(17) Neudecker, B. J.; Dudney, N. J.; Bates, J. B. "Lithium-Free" Thin-Film Battery with In Situ Plated Li Anode. *J. Electrochem. Soc.* **2000**, *147* (2), 517.
(18) Zor, C.; Turrell, S. J.; Uyanik, M. S.; Afyon, S. Lithium Plating and Stripping: Toward Anode-Free Solid-State Batteries. *Adv. Energy Sustainability Res.* **2023**, *5* (8), 2300001.
(19) Fuchs, T.; Becker, J.; Haslam, C. G.; Lerch, C.; Sakamoto, J.; Richter, F. H.; Janek, J. Current-Dependent Lithium Metal Growth Modes in "Anode-Free" Solid-State Batteries at the Cu|LLZO Interface. *Adv. Energy Mater.* **2023**, *13* (1), 2203174.
(20) Singh, V. K.; Schuler, J.; Ortmann, T.; Ziegler, M.; Janek, J.; Nazar, L. F. High Coulombic Efficiency Plating and Stripping of Sodium for Reservoir-Free Sodium Solid-State Batteries at Low Stack Pressure. *ACS Energy Lett.* **2025**, *10* (8), 3663–3669.
(21) Krauskopf, T.; Richter, F. H.; Zeier, W. G.; Janek, J. Physicochemical Concepts of the Lithium Metal Anode in Solid-State Batteries. *Chem. Rev.* **2020**, *120* (15), 7745–7794.
(22) Eckhardt, J. K.; Fuchs, T.; Burkhardt, S.; Klar, P. J.; Janek, J.; Heiliger, C. 3D Impedance Modeling of Metal Anodes in Solid-State Batteries-Incompatibility of Pore Formation and Constriction Effect in Physical-Based 1D Circuit Models. *ACS Appl. Mater. Interfaces* **2022**, *14* (37), 42757–42769.
(23) Eckhardt, J. K.; Klar, P. J.; Janek, J.; Heiliger, C. Interplay of Dynamic Constriction and Interface Morphology between Reversible Metal Anode and Solid Electrolyte in Solid State Batteries. *ACS Appl. Mater. Interfaces* **2022**, *14* (31), 35545–35554.
(24) Kim, J.-S.; Yoon, G.; Kim, S.; Sugata, S.; Yashiro, N.; Suzuki, S.; Lee, M.-J.; Kim, R.; Badding, M.; Song, Z.; Chang, J.; Im, D. Surface engineering of inorganic solid-state electrolytes via interlayers strategy for developing long-cycling quasi-all-solid-state lithium batteries. *Nat. Commun.* **2023**, *14* (1), 782.
(25) Lee, Y.-G.; Fujiki, S.; Jung, C.; Suzuki, N.; Yashiro, N.; Omoda, R.; Ko, D.-S.; Shiratsuchi, T.; Sugimoto, T.; Ryu, S.; Ku, J. H.; Watanabe, T.; Park, Y.; Aihara, Y.; Im, D.; Han, I. T. High-energy long-cycling all-solid-state lithium metal batteries enabled by silver–carbon composite anodes. *Nat. Energy* **2020**, *5* (4), 299–308.
(26) Haslam, C.; Sakamoto, J. Stable Lithium Plating in "Lithium Metal-Free" Solid-State Batteries Enabled by Seeded Lithium Nucleation. *J. Electrochem. Soc.* **2023**, *170* (4), 040524.
(27) Suzuki, N.; Yashiro, N.; Fujiki, S.; Omoda, R.; Shiratsuchi, T.; Watanabe, T.; Aihara, Y. Highly Cyclable All-Solid-State Battery with Deposition-Type Lithium Metal Anode Based on Thin Carbon Black Layer. *Adv. Energy Sustainability Res.* **2021**, *2* (11), 2100066.
(28) Kim, S.; Jung, C.; Kim, H.; Thomas-Alyea, K. E.; Yoon, G.; Kim, B.; Badding, M. E.; Song, Z.; Chang, J.; Kim, J.; Im, D.; Kang, K. The Role of Interlayer Chemistry in Li-Metal Growth through a Garnet-Type Solid Electrolyte. *Adv. Energy Mater.* **2020**, *10* (12), 1903993.
(29) Park, S. H.; Jun, D.; Jung, J. E.; Lee, S. G.; Lee, G. H.; Lee, Y. J. Clarification of Li deposition behavior on anodes with a porous interlayer in Li-free all-solid-state batteries. *J. Mater. Chem. A* **2022**, *10* (41), 21995–22006.
(30) Tseng, K.-T.; Lee, K.; Sakamoto, J. Enabling "Sodium–Metal-Free" Manufacturing of Solid-State Batteries. *ACS Energy Lett.* **2024**, *9* (9), 4544–4549.
(31) Lowack, A.; Grun, P.; Anton, R.; Auer, H.; Nikolowski, K.; Partsch, M.; Kusnezoff, M.; Michaelis, A. Sputtered Zero-Excess Electrodes with Metallic Seed Layers for Solid-State Sodium Batteries. *Batteries Supercaps* **2025**, *8* (5), e202400364.
(32) Kim, S.; Yoon, G.; Jung, S.-K.; Park, S.; Kim, J.-S.; Yoon, K.; Lee, S.; Kang, K. High-Power Hybrid Solid-State Lithium–Metal Batteries Enabled by Preferred Directional Lithium Growth Mechanism. *ACS Energy Lett.* **2023**, *8* (1), 9–20.

https://doi.org/10.1021/acselectrochem.6c00121
ACS Electrochem. 2026, 2, 1887–1903

(33) Sandoval, S. E.; Haslam, C. G.; Vishnugopi, B. S.; Liao, D. W.; Yoon, J. S.; Park, S. H.; Wang, Y.; Mitlin, D.; Hatzell, K. B.; Siegel, D. J.; Mukherjee, P. P.; Dasgupta, N. P.; Sakamoto, J.; McDowell, M. T. Electro-chemo-mechanics of anode-free solid-state batteries. *Nat. Mater.* **2025**, *24* (5), 673–681.
(34) Da Ko, Y.; Kim, H. J.; Park, H.; Kim, E.; Kim, H. Correlation between the Microstructure of the Carbon Protective Layer and Cycle Performance of Anode-Free All-Solid-State Lithium-Ion Batteries. *ACS Nano* **2025**, *19* (17), 16957–16966.
(35) Futscher, M. H.; Amelal, T.; Sastre, J.; Müller, A.; Patidar, J.; Aribia, A.; Thorwarth, K.; Siol, S.; Romanyuk, Y. E. Influence of amorphous carbon interlayers on nucleation and early growth of lithium metal at the current collector-solid electrolyte interface. *J. Mater. Chem. A* **2022**, *10* (29), 15535–15542.
(36) Park, S. H.; Naik, K. G.; Vishnugopi, B. S.; Mukherjee, P. P.; Hatzell, K. B. Lithium Kinetics in Ag–C Porous Interlayer in Reservoir-Free Solid-State Batteries. *Adv.Energy Mater.* **2025**, *15* (16), 2405129.
(37) Liao, D. W.; Zeng, D.; Mulla, M.; Madanchi, A.; Kawakami, H.; Aihara, Y.; Aotani, K.; Thouless, M. D.; Dasgupta, N. P. Effects of Interfacial Adhesion on Lithium Plating Location in Solid-State Batteries with Carbon Interlayers. *Adv. Mater.* **2025**, *37* (29), e2502114.
(38) Sun, C.; Li, Y.; Sun, Z.; Yuan, X.; Jin, H.; Zhao, Y. Ferroelectric interface for efficient sodium metal cycling in anode-free solid-state batteries. *Mater. Today* **2024**, *80*, 395–405.
(39) Ruan, J.; Hu, J.; Li, Q.; Luo, S.; Yang, J.; Liu, Y.; Song, Y.; Zheng, S.; Sun, D.; Fang, F.; Wang, F. Current collector interphase design for high-energy and stable anode-less sodium batteries. *Nat. Sustainability* **2025**, *8* (5), 530–541.
(40) Matei Ghimbeu, C.; Beda, A.; Réty, B.; El Marouazi, H.; Vizintin, A.; Tratnik, B.; Simonin, L.; Michel, J.; Abou-Rjeily, J.; Dominko, R. Review: Insights on Hard Carbon Materials for Sodium-Ion Batteries (SIBs): Synthesis – Properties – Performance Relationships. *Adv. Energy Mater.* **2024**, *14* (19), 2303833.
(41) Cao, H.; Meng, L.; Qin, C.; Han, Z.; Yang, L.; Dong, H.; Hou, Y.; Xiao, C.; Wang, J.; Guo, J. Linking the size of hard carbon particles with electrochemical response in sodium ion storage. *Appl. Surf. Sci.* **2024**, *678*, 161126.
(42) Xiao, S.; Guo, Y.-J.; Chen, H.-X.; Liu, H.; Lei, Z.-Q.; Huang, L.-B.; Jin, R.-X.; Su, X.-C.; Zhang, Q.; Guo, Y.-G. Insight into the Role of Closed-Pore Size on Rate Capability of Hard Carbon for Fast-Charging Sodium-Ion Batteries. *Adv. Mater.* **2025**, *37* (28), e2501434.
(43) Liu, F.; Chen, Z.; Li, Y.; Fu, L.; Ju, J.; Ma, J.; Sun, Y. Sodium plating on hard carbon anodes in sodium-ion batteries: mechanisms, detection methods, and mitigation strategies. *Nanoscale Horiz.* **2025**, *11*, 62–84.
(44) Pierson, H. O. *Handbook of carbon, graphite, diamond, and fullerenes:Properties, processing, and applications*; Materials science and process technology series. Electronic materials and process technology; Noyes Publications, **1993.**
(45) Gold, V.; McNaught, A. *The IUPAC Compendium of Chemical Terminology*; International Union of Pure and Applied Chemistry (IUPAC), **2025**.
(46) Ruland, W.; Smarsly, B. X-ray scattering of non-graphitic carbon: an improved method of evaluation. *Appl. Crystallogr.* **2002**, *35* (5), 624–633.
(47) Liu, W.; Tian, X.; Ming, Y.; Shi, P.; He, X. Review of Hard Carbon Anodes for Sodium-Ion Batteries: Mechanisms, Precursors, and Modification Strategies. *Energy Technol.* **2025**, *13* (12), 2500173.
(48) Chu, C.; Wang, N.; Li, L.; Lin, L.; Tian, F.; Li, Y.; Yang, J.; Dou, S.; Qian, Y. Uniform nucleation of sodium in 3D carbon nanotube framework via oxygen doping for long-life and efficient Na metal anodes. *Energy Storage Mater.* **2019**, *23*, 137–143.
(49) Sánchez-González, J.; Macías-García, A.; Alexandre-Franco, M. F.; Gómez-Serrano, V. Electrical conductivity of carbon blacks under compression. *Carbon* **2005**, *43* (4), 741–747.
(50) Pantea, D.; Darmstadt, H.; Kaliaguine, S.; Roy, C. Electrical conductivity of conductive carbon blacks: influence of surface chemistry and topology. *Appl. Surf. Sci.* **2003**, *217* (1-4), 181–193.
(51) Krauskopf, T.; Hartmann, H.; Zeier, W. G.; Janek, J. Toward a Fundamental Understanding of the Lithium Metal Anode in Solid-State Batteries-An Electrochemo-Mechanical Study on the Garnet-Type Solid Electrolyte $Li_{6.25}Al_{0.25}La_3Zr_2O_{12}$. *ACS Appl. Mater. Interfaces* **2019**, *11* (15), 14463–14477.
(52) Ortmann, T.; Burkhardt, S.; Eckhardt, J. K.; Fuchs, T.; Ding, Z.; Sann, J.; Rohnke, M.; Ma, Q.; Tietz, F.; Fattakhova-Rohlfing, D.; Kübel, C.; Guillon, O.; Heiliger, C.; Janek, J. Kinetics and Pore Formation of the Sodium Metal Anode on NASICON-Type $Na_{3.4}Zr_2Si_{2.4}P_{0.6}O_{12}$ for Sodium Solid-State Batteries. *Adv. Energy Mater.* **2023**, *13* (5), 2202712.
(53) Pei, A.; Zheng, G.; Shi, F.; Li, Y.; Cui, Y. Nanoscale Nucleation and Growth of Electrodeposited Lithium Metal. *Nano Lett.* **2017**, *17* (2), 1132–1139.
(54) Liu, Y.; Xu, X.; Sadd, M.; Kapitanova, O. O.; Krivchenko, V. A.; Ban, J.; Wang, J.; Jiao, X.; Song, Z.; Song, J.; Xiong, S.; Matic, A. Insight into the Critical Role of Exchange Current Density on Electrodeposition Behavior of Lithium Metal. *Adv. Sci.* **2021**, *8* (5), 2003301.
(55) Park, S. H.; Ayyaswamy, A.; Gjerde, J.; Andrews, W. B.; Vishnugopi, B. S.; Drakopoulos, M.; Vo, N. T.; Zhong, Z.; Thornton, K.; Mukherjee, P. P.; Hatzell, K. B. Filament-Induced Failure in Lithium-Reservoir-Free Solid-State Batteries. *ACS Energy Lett.* **2025**, *10* (3), 1174–1182.
(56) Müller, A.; Paravicini, L.; Morzy, J.; Krause, M.; Casella, J.; Osenciat, N.; Futscher, M. H.; Romanyuk, Y. E. Influence of Au, Pt, and C Seed Layers on Lithium Nucleation Dynamics for Anode-Free Solid-State Batteries. *ACS Appl. Mater. Interfaces* **2024**, *16* (1), 695–703.
(57) Liao, D. W.; Cho, T. H.; Sarna, S.; Jangid, M. K.; Kawakami, H.; Kotaka, T.; Aotani, K.; Dasgupta, N. P. Interfacial dynamics of carbon interlayers in anode-free solid-state batteries. *J. Mater. Chem. A* **2024**, *12* (10), 5990–6003.
(58) Paul, P. P.; Thampy, V.; Cao, C.; Steinrück, H.-G.; Tanim, T. R.; Dunlop, A. R.; Dufek, E. J.; Trask, S. E.; Jansen, A. N.; Toney, M. F.; Nelson Weker, J. Quantification of heterogeneous, irreversible lithium plating in extreme fast charging of lithium-ion batteries. *Energy Environ. Sci.* **2021**, *14* (9), 4979–4988.
(59) Tanim, T. R.; Paul, P. P.; Thampy, V.; Cao, C.; Steinrück, H.-G.; Nelson Weker, J.; Toney, M. F.; Dufek, E. J.; Evans, M. C.; Jansen, A. N.; Polzin, B. J.; Dunlop, A. R.; Trask, S. E. Heterogeneous Behavior of Lithium Plating during Extreme Fast Charging. *Cell Rep. Phys. Sci.* **2020**, *1* (7), 100114.
(60) Kazyak, E.; Wang, M. J.; Lee, K.; Yadavalli, S.; Sanchez, A. J.; Thouless, M. D.; Sakamoto, J.; Dasgupta, N. P. Understanding the electro-chemo-mechanics of Li plating in anode-free solid-state batteries with operando 3D microscopy. *Matter* **2022**, *5* (11), 3912–3934.
(61) Zhang, X.; Wang, Q. J.; Peng, B.; Wu, Y. Pressure-Driven and Creep-Enabled Interface Evolution in Sodium Metal Batteries. *ACS Appl. Mater. Interfaces* **2021**, *13* (22), 26533–26541.
(62) Wang, M. J.; Chang, J.-Y.; Wolfenstine, J. B.; Sakamoto, J. Analysis of elastic, plastic, and creep properties of sodium metal and implications for solid-state batteries. *Materialia* **2020**, *12*, 100792.
(63) Feng, X.; Li, Y.; Li, Y.; Liu, M.; Zheng, L.; Gong, Y.; Zhang, R.; Wu, F.; Wu, C.; Bai, Y. Unlocking the local structure of hard carbon to grasp sodium-ion diffusion behavior for advanced sodium-ion batteries. *Energy Environ. Sci.* **2024**, *17* (4), 1387–1396.
(64) Liu, Y.; Liu, X.; Zhang, G.; Shi, X.; Zhang, P.; Fan, Y.; Huang, Y.; Zhang, R. "Carbon in Metal" Anode with High Processability for Sodium Metal Batteries. *ACS Appl. Mater. Interfaces* **2023**, *15* (22), 26691–26699.
(65) Ma, Q.; Tsai, C.-L.; Wei, X.-K.; Heggen, M.; Tietz, F.; Irvine, J. T. S. Room temperature demonstration of a sodium superionic conductor with grain conductivity in excess of 0.01 S cm −1 and its primary applications in symmetric battery cells. *J. Mater. Chem. A* **2019**, *7* (13), 7766–7776.
(66) Eckhardt, J. K.; Fuchs, T.; Burkhardt, S.; Klar, P. J.; Janek, J.; Heiliger, C. Guidelines for Impedance Analysis of Parent Metal

https://doi.org/10.1021/acselectrochem.6c00121
ACS Electrochem. 2026, 2, 1887–1903

Anodes in Solid-State Batteries and the Role of Current Constriction at Interface Voids, Heterogeneities, and SEI. *Adv. Mater. Interfaces* **2023**, *10* (8), 2202354.
(67) Irvine, J. T. S.; Sinclair, D. C.; West, A. R. Electroceramics: Characterization by Impedance Spectroscopy. *Adv. Mater.* **1990**, *2* (3), 132–138.
(68) Vadhva, P.; Hu, J.; Johnson, M. J.; Stocker, R.; Braglia, M.; Brett, D. J. L.; Rettie, A. J. E. Electrochemical Impedance Spectroscopy for All-Solid-State Batteries: Theory, Methods and Future Outlook. *ChemElectroChem* **2021**, *8* (11), 1930–1947.
(69) Li, M.; Mao, A.; Guan, Q.; Saiz, E. Nature-inspired adhesive systems. *Chem. Soc. Rev.* **2024**, *53* (16), 8240–8305.
(70) Seymour, I. D.; Quérel, E.; Brugge, R. H.; Pesci, F. M.; Aguadero, A. Understanding and Engineering Interfacial Adhesion in Solid-State Batteries with Metallic Anodes. *ChemSusChem* **2023**, *16* (12), e202202215.
(71) Antonio, P.; Mittal, K. L.; *Handbook of adhesive technology*, ; CRC Press, **2018**.
(72) McBain, J. W.; Hopkins, D. G. On Adhesives and Adhesive Action. *J.of Phys. Chem.* **1925**, *29* (2), 188–204.
(73) Park, J.; Jung, J.; Yang, S.; Kim, D. H.; Lee, J. B.; Oh, J. A. S.; Yang, H.; Nashiru, M.; Huang, C.-J.; Meng, Y. S. Realizing Low-Pressure Operation of All-Solid-State Lithium–Sulfur Batteries Enabled by Carbon-Coated Current Collectors. *Adv. Energy Mater.* **2025**, *16* (1), e04272.
(74) Zhang, S.; Hu, B.; Geng, Z.; Gao, X.; Spencer-Jolly, D.; Melvin, D. L.; Ning, Z.; Li, G.; Jenkins, M.; Wang, L.; Gao, H.; Pu, S. D.; Marrow, T. J.; Monroe, C. W.; Bruce, P. G. Influence of contouring the lithium metal/solid electrolyte interface on the critical current for dendrites. *Energy Environ. Sci.* **2024**, *17* (4), 1448–1456.
(75) Hasegawa, G.; Hattori, M.; Nakanishi, K.; Hayashi, K. Co-continuous hard Carbon/NASICON electrodes for all-solid-state batteries: Insights into structural stability and interfacial Na-ion transfer. *Energy Storage Mater.* **2025**, *80*, 104437.
(76) Wang, M. J.; Carmona, E.; Gupta, A.; Albertus, P.; Sakamoto, J. Enabling "lithium-free" manufacturing of pure lithium metal solid-state batteries through in situ plating. *Nat. Commun.* **2020**, *11* (1), 5201.
(77) Kasemchainan, J.; Zekoll, S.; Spencer Jolly, D.; Ning, Z.; Hartley, G. O.; Marrow, J.; Bruce, P. G. Critical stripping current leads to dendrite formation on plating in lithium anode solid electrolyte cells. *Nat. Mater.* **2019**, *18* (10), 1105–1111.
(78) Krauskopf, T.; Dippel, R.; Hartmann, H.; Peppler, K.; Mogwitz, B.; Richter, F. H.; Zeier, W. G.; Janek, J. Lithium-Metal Growth Kinetics on LLZO Garnet-Type Solid Electrolytes. *Joule* **2019**, *3* (8), 2030–2049.
(79) Tanaka, S.; Nishiyama, N.; Egashira, Y.; Ueyama, K. Synthesis of ordered mesoporous carbons with channel structure from an organic-organic nanocomposite. *Chem. Commun.* **2005** (*16*), 2125–2127.
(80) Osswald, O.; Smarsly, B. M. OctCarb—A GNU Octave Script for the Analysis and Evaluation of Wide-Angle Scattering Data of Non-Graphitic Carbons. *C* **2022**, *8* (4), 78.
(81) Badaczewski, F.; Loeh, M. O.; Pfaff, T.; Dobrotka, S.; Wallacher, D.; Clemens, D.; Metz, J.; Smarsly, B. M. Peering into the structural evolution of glass-like carbons derived from phenolic resin by combining small-angle neutron scattering with an advanced evaluation method for wide-angle X-ray scattering. *Carbon* **2019**, *141*, 169–181.
(82) Faber, K.; Badaczewski, F.; Ruland, W.; Smarsly, B. M. Investigation of the Microstructure of Disordered, Non-graphitic Carbons by an Advanced Analysis Method for Wide-Angle X-ray Scattering. *Zeitschrift für anorgische und allgemeine Chemie* **2014**, *640* (15), 3107–3117.

https://doi.org/10.1021/acselectrochem.6c00121
ACS Electrochem. 2026, 2, 1887−1903